Mechanical coupling of compartments drives polarity and patterning of mouse auditory epithelium

Anubhav Prakash[1,2,#], Sukanya Raman[1], Raman Kaushik[1], Anton S Iyer[1], Raj K. Ladher[1,#]

1. National Centre for Biological Sciences, Tata Institute of Fundamental Research, GKVK PO, Bellary Road, Bangalore, India, 560065

2. Trivedi School of Biosciences, Ashoka University, Plot No. 2, Rajiv Gandhi Education City, National Capital Region P.O. Rai, Sonipat Haryana-131029

Authors for Correspondence

Anubhav Prakash
anubhav.prakash@ashoka.edu.in

Raj K. Ladher
rajladher@ncbs.res.in

Keywords: Planar Cell Polarity, Organogenesis, Cadherin, Inner Ear, Compartments

ABSTRACT

The information that drives morphogenesis depends not only on genetically encoded cellular properties, but also emerges from the interaction between these cell behaviours. This information is spatio-temporally implemented to make tissue shape and order robust and reproducible during development. What are the principles for organising this information? The mouse auditory epithelium, the organ of Corti (OC) is an excellent system to investigate this. A central domain senses sound information through mechanosensory hair cells (HC), part of a mosaic with supporting cells (SC). This is flanked by non-sensory domains. These domains undergo cellular rearrangements as they become ordered and elongate. How cellular properties are coordinated across domains and how these contribute to tissue shape is unknown. Here, we find adhesion codes, established through morphogen patterning, define OC domains as compartments. Cells in each compartment exhibit distinct patterns of ordering. By perturbing cellular rearrangements in individual compartments, we find that compartment-specific ordering can contribute to overall tissue architecture. Perturbation of cell order within a compartment also affects the organisation in another. Using vinculin mutants, we show that inter-compartment coupling is, in part, mechanical. Our work suggests that compartments and their coupling can organise morphogenetic information in space and time during organogenesis.

INTRODUCTION

The reproducibility and robustness of morphogenesis result from carefully implemented developmental instructions. These instructions are organised into spatial hierarchies that structure pattern information. From an initial large embryonic field, a combination of signalling cues, gene networks, and self-organising mechanisms establishes compartments [1,2]. The use of compartments in development is widespread, and interactions between compartments are a recurring theme [3-5]. Compartments do not mix, and it is known that compartment interfaces can be induced to adopt new fates and may express, for example, signalling molecules that influence bordering regions [6,7]. Despite the use of compartments in tissue patterning, their role during tissue morphogenesis needs to be clarified.

The mammalian cochlea is a highly specialised organ responsible for detecting and transducing sound across a wide spectrum of frequencies [8,9]. To accommodate the frequency range, the cochlea is spiral-shaped [10]. The number of turns and their pitch are characteristic of a species [11]. The cochlea houses the auditory epithelium, the organ of Corti (OC). The OC is a composite epithelium comprising several sensory and non-sensory domains (Fig. 1A)[12]. The sensory region consists of two types of mechanosensory hair cells that are organised into 4 rows. A single row of inner HC (IHC) and 3 rows of outer HC (OHC). Various types of supporting cells (SC) surround the hair cells. These include the Pillar Cells (PC), which separate the IHC and OHC domains. HC are also intrinsically polar, with an asymmetric hair bundle on their apical surface. This polarity is aligned to a tissue-wide axis (Fig. S1A). The sensory region is flanked by non-sensory domains. A medial non-sensory domain, known as Kölliker's organ (KO) is found medial to the IHC domain. The lateral non-sensory domain, which includes Hensen's and Claudius' cells, is lateral to the OHC domain (Fig. S1A).

The cochlea is initially apparent as a ventral out-pocketing of the otocyst. Radial patterning of the nascent cochlear duct by morphogen signalling, establishes non-sensory and

sensory domains of the OC [12,13]. The cells in the sensory region become post-mitotic and, through juxtracrine signalling, differentiate into a mosaic of HC and SC [14,15]. These initial cellular patterns are often imprecise. However, recent studies have provided evidence for mechanical mechanisms that impart order onto these domains, leading to both spatial order and planar polarity [16-20]. Both experimental approaches and mathematical modelling have shown that the differential tension among junctions driven by adhesion molecules and myosin activity could organise HC and SC spatial organisation [19,20]. Moreover, differential tension at HC-SC and SC-SC junctions also aligns the polarity of each HC to the tissue axis [20]. While cells locally coordinate in the sensory domain, large-scale convergence and extension (CE) movements cause the OC to elongate, also contributing to morphogenesis [21-24]. Additional differences across the medial to lateral extent of the cochlear duct also contribute to the overall shape[25,26]. Thus, local domain-specific processes that order HC spatially and orientationally must integrate with large-scale tissue remodelling. How they integrate is not known.

We have investigated this question using the developing mouse OC. We show that the OC compartmentalises into smaller domains through a combinatorial expression of Cadherin 1, 2, and 4 and Nectins. The adhesion code of each domain ensures their integrity, such that they develop as compartments. These compartments have two properties. First, each develops a discrete cellular organisation driven by planar cell polarity-mediated non-muscle myosin II activity. Second, using cell-type-specific knockouts of Vangl2 we show that cellular organisation within each compartment influences organisation in another compartment. Using mice mutant for the junctional force transmission component Vinculin, we show that compartment coupling has a mechanical component. Our work suggests that compartments and their coupling provide a framework to organise morphogenetic information, enabling the integration of cellular ordering with large-scale tissue remodelling. Given the widespread use

of compartments, inter-compartment coupling is likely a fundamental feature of the morphogenesis of many developing tissues and organs.

RESULTS

Cellular organisation is preserved during convergent extension

By E15.5, domain organisation in the OC is apparent. The pattern of organisation within the sensory regions is apparent by E18.5 (Fig. 1A, Fig. S1A) [27,28]. During this period, the cochlea also undergoes convergence and extension movements, doubling in length (from 2734±33µm at E15.5 to 4702±277µm at E18.5) (Fig S1B,C). As these movements involve extensive cellular rearrangements [21-23], we asked whether we could detect perturbation in domain organisation. The lateral non-sensory domains consists of Hensen's (HnC) and Claudius (CS) cells. Even at E15.5, HnC are already distinct as a large cell type abutting the outer border cells of the OHC domain (Fig. S1D). Cells of the KO are apparent as homogenous epithelial cells, abutting the medial sensory domain. At E 18.5 the position of the non-sensory domains are perserved (Fig. S1D).

We next asked if the relative positions of the medial and lateral sensory domains were preserved. We used p75NTR, a marker for pillar cells that separates the medial and lateral sensory domains [29]. We also examined the expression of brain lipid binding-protein (BLBP), a marker of inner phalangeal cells (IPC) [30,31], an SC type that intercalates IHC, and Myosin 7a, a marker for HC. Even at E15.5, p75NTR shows expression in a distinct row of cells that marks the border between medial and lateral sensory domains (Fig. S1E). BLBP also forms a row of expression at these stages (Fig. S1G). At E18.5, immunostaining OC for markers of HC, pillar cells, inner phalangeal cells showed that the relative position of cell types is maintained during OC elongation, suggesting the preservation of the sensory domains (Fig S1D-G).

We next asked whether OC domain organisation was perturbed in mouse mutants where convergence and extension-mediated elongation is perturbed. Mice mutant for the core PCP protein, Vangl2, show defects in HC planar cell polarity and convergence and extension

(CE) movements [32-35]. Homozygous *looptail* mutants of Vangl2 (referred as *Vangl2*$^{Lp/Lp}$) have a cochlea 2/3rd the length of littermate controls (*Vangl2*$^{Lp/+}$ 5010±41µm and *Vangl2*$^{Lp/Lp}$ 3238±185µm) (Fig 1B, C). Immunostaining for molecular markers for HCs (Fig 1D), IPC (Fig 1E), Pillar cells (Fig1F) and the distinction in the morphological features of non-sensory cell types (Fig 1G, H) revealed the relative position of cell types are maintained in the *Vangl2*$^{Lp/Lp}$ mutants at basal, medial and apical edge of OC (Fig. 1D-G, Fig. S2). The preservation of domain organisation, even when CE movements are perturbed, suggests a mechanism that maintains domain integrity in the OC.

Adhesion Code defines compartments in the OC

Studies of mixed cultures of adhesion-molecule expressing cells and extending into those on gastrulating amphibian embryos and the fish neural tube have shown that differential interactions between adhesion molecules can segregate cells into domains [36-39]. Differential expression of cadherins and nectins have been observed in the sensory domain, leading us to examine their expression in the entire OC [17,23,40,41]. We investigated 3 cadherin family members, Cdh1, Cdh2 and Cdh4 (E-, N- and R- cadherin respectively), and nectin-1 and -2, as well as the tight junction protein ZO-1.

AE18.5, ZO1 and Nectin 2 are localised on the apical junctions of all the cells of the OC (Figure 2A, S3A). Nectin 1 is expressed only on the HC-SC junctions (Figure S3B). The expression of Cdh1 was found in the junctions of cells in the lateral domain of the OC encompassing lateral sensory and non-sensory domain (Figure 2B). A faint expression of Cdh1 could also be seen in a subset of Kölliker organ cells bordering the medial sensory domain domain. Cdh2 was expressed in the medial sensory and non-sensory domains (Figure 2C). The expression of Cdh4 was similar to Cdh2, although expression was not detected in IPH cells (Figure 2D). We defined this combinatorial expression of Cadherins and Nectins as

an adhesion code, which can be superimposed onto the domains of OC. We hypothesised that the adhesion code maintains the integrity of OC domains during CE.

To test the role of cadherins in OC domain organisation, we sought to attenuate their interaction using blocking antibodies. To do so, we used an ex-vivo organ culture method to culture E16.5 cochlea in the presence of these antibodies (Fig. 2E, F). The 5D3 antibody, blocks Cdh1 interactions [42]. Treatment with this leads to the disruption in the organisation of lateral regions of OC (Figure 2G-J). The checkerboard organisation of HC and DC in the lateral sensory domain was perturbed, with frequent HC-HC contacts. In control explants, the OHC is separated from Hensen's Cells by outer border cells; however, in the samples incubated in the Cdh1 blocking antibody, direct interfaces between OHC and HnC were observed (Fig 2I). Despite the lateral domains showing perturbations in their organisation, the medial sensory and non-sensory domains did not (Fig 2I). To block Cdh2 interactions, we cultured cochlea in the presence of the 6B3 antibody[43]. Such cultured explants showed perturbation in the medial domain of OC (Fig 2K, L). Here, IHC and IPC organisation was disrupted, and resulted in the drifting of IHC into the KO domain and the disorganisation of IPH and inner border cells (Fig 2K, L). The effect on the lateral regions of the OC were negligible.

As an alternative approach to perturbing the adhesion code, we took our cue from studies in the Drosophila wing disc and zebrafish neural tube [36,44]. Here, the combinatorial expression of adhesion molecules is controlled by morphogen signalling, which also controls cell fate and organisation. Similarly, the signals that radially pattern the cochlea into domains may also control the expression of cadherins. Radial patterning occurs before HC differentiation, which is initiated at around E14.5 [12]. At these stages of development, Cdh1, 2 and 4 are localised to distinct regions (Fig S3C-F). Similar to the localisation at E18.5, at E14.5, Cdh1 shows expression in the lateral regions of the OC, with a faint strip of

expression detected medially. Cdh2 and Cdh4 are restricted to the medial OC (Fig S3C-F). To disrupt this pattern, we sought to disrupt one of the morphogen signals involved. FGF signalling, through the Fgfr1, influences radial patterning [45,46]. We find that the reciprocal localisation of Cdh1 and Cdh2 is abolished in conditional deletions of *Fgfr1* from the inner ear (*Six1enh21Cre*$^{+/-}$*::Fgfr1*$^{fl/fl}$) at E14.5 (Fig S3G, H).

To understand the consequence of perturbing the adhesion code, we examined E18.5 Fgfr1 mutant embryos. As previously described, the sensory cells from these mutants form clusters called islands along the length of OC [47,48] [45,46] (Figure S4A). We hypothesised that early disruption of adhesion code may contribute to this island phenotype. At E18.5, we observed that in *Fgfr1* mutants, the lateral non-sensory domain now expressed Cdh2, in addition to Cdh1. Moreover, the presumptive IHC, that is, those HCs that are closer to KO, now also expressed Cdh1 in addition to Cdh2 (Fig S4C, D). We observe HCs infiltrate both the KO domain, and the lateral non-sensory domain in the Fgfr1 mutants (Fig S4E).

Our data suggest that the adhesion code preserves domain integrity in the OC during the CE movements. We reasoned that maintaining the adhesion code underlies the preservation of domain organisation in *Vangl2*$^{Lp/Lp}$ mutants. Accordingly, we find that the expression domains of Cdh1, Cdh2 and Cdh4 are unaffected in these mutants, even though CE is disrupted (Fig. S5).

Sensory and non-sensory domain acquire discrete ordering

The sub-division of the OC into domains that retain their integrity during development is reminiscent of compartments. Compartments, as a developmental unit, have been studied in Drosophila imaginal discs and the hindbrain, trachea, ovarian follicles, and somites [3,4,49]. These studies suggest that compartments have genetic and cellular profiles that are distinct from neighbouring compartments. This would lead to distinct compartment-specific

morphologies. By investigating their phenotypic characteristics, we asked if the OC domains could be considered compartments.

Using phalloidin to mark F-actin, to segment cells, and Arl13b to mark kinocilia and measure HC polarity, we measured cell shape and orientation along the OC between E15.5 to E18.5 (Fig. 3A, Fig. S6A-C). We started with lateral sensory domain: This consists of 3 rows of OHCs intercalated by a SC type called Dieter's cells. Between E15.5 and E18.5, the OHC apical surface area and circularity increased (Fig. S6E, F). These changes are accompanied by an increase in the hexagonal arrangement of OHCs between three rows, which is apparent as a refinement of the row-wise alignment of OHC (Fig. S7A-G). During this period, the hair bundle of OHCs becomes planar polarised. We find that as OHCs become hexatically ordered, their planar polarity aligns to the tissue axis (Fig. S7H, I).

The medial sensory domain contains a single row of IHC intercalated by BLBP-expressing IPhCs. In contrast to the lateral sensory domain, the medial sensory domain is developmentally advanced, with the polarity of the hair bundle apparent a day earlier than OHC from the same region of the cochlea[50]. An increase in apical surface area and circularity of IHC correlates with the row-wise organisation of IHCs and an increase in alignment of planar polarity (Fig. S7A-H, J, K).

To understand how the changes in cellular organisation within each compartment affects the shape of the sensory domain, we measured its dimensions. We observed that between E15.5 and E18.5, the width of both medial and lateral sensory domains increased at the base and decreased at the apical turn of OC (Fig S8A-C). This was reflected in the width of combined sensory region (Fig 3A, B). The change in sensory domain width was accompanied with an increase in length between E15.5 to E18.5, indicative of cell rearrangement-driven convergence and extension (Fig. S1C). In epithelia, cellular rearrangements are driven by neighbour exchange. During this, vertices are formed between 4

or more cells, which provides a measure of this process [22]. At E15.5, 1/3rd of all vertices in the sensory domain are between 4 or more cells (Fig. S8D, E). This decreases significantly by E18.5, such that only 20% of vertices are between 4 or more cells (Fig. S8D, E).

We next turned to medial non-sensory domain, the KO. Consistent with the increase in cochlear length, the KO also elongates twice its length along the base-apex axis of the cochlea. The width of the KO decreased at the base and the middle turn of cochlea between E15.5 and E18.5 (Fig. 3C, D). At E15.5, the KO consists of cells with a varied apical surface area and a roughly symmetrical aspect ratio (AR=0.87±0.12) closer to 1 (Fig. 3D-F, Fig. S9A-G). A small population of cells show an asymmetric elongation and have their long axis aligned perpendicular to the mediolateral axis of the OC (Fig. 3D, G, Fig. S9A-D). By E18.5, cells with a smaller apical surface area are observed closer to the medial edge (mKO) (Fig. 3D, G, Fig. S9A-G). These cells are elongated, with the long axis parallel to the tissue axis. In contrast, cells of the lateral KO (lKO), closer to the medial sensory domain, have a larger surface area and are elongated orthogonal to the tissue axis (Figure 3E, Fig. S9A-G). Our length and width measurements suggest that KO cells undergo rearrangements. To assess this, we identified the number of 4-cell vertices. At E15.5 cells in the mKO and lKO also showed differences in proportion of vertices with 4 or more cells; suggesting a higher rate of cellular reorganisation in the mKO compared to the lKO (Fig. S9H). The proportion of vertices with 4 or more cells decreased in the lKO by E18.5 while at mKO showed the proportion of vertices with 4 or more cells at E18.5 remained equivalent to the numbers observed at E15.5 (Fig. S9H). This data shows the cells in the KO undergo cellular reorganisation during development. KO cells closer to the medial edge are elongated along the base-to-apex axis and show more 4-cell vertices. Lateral KO cells become larger between E15.5 to E18.5 and are elongated along the mediolateral axis, orthogonal to the mKO cells. There is less cell rearrangement in this domain. These changes in the shape and size of cells

are accompanied by a convergence of the KO domain along the mediolateral axis and the extension along the base-to-apex axis. In the lateral non-sensory domain, we observe an increase in apical surface area and shape index of HnC and CsC (Fig. S10).

The development of domain-specific morphologies, combined with their distinct cadherin expression profiles, suggest that the OC domains can be considered as compartments. Along with individual cellular features of each compartment, compartments also show large tissue-scale changes, restricted to each compartment. This is particularly prominent in the medial and lateral sensory and KO compartments. The appearance of four cell vertices suggests cellular rearrangements drive these tissue-scale changes.

Vangl2 regulates tissue-scale compartment-specific behaviours

To understand the mechanisms underlying cellular rearrangements, we turned to PCP proteins. Numerous studies suggest that planar cell polarity proteins can regulate cellular rearrangements [20,51-57]. We thus immunostained OC for Vangl2. In the E18.5 medial sensory compartment, Vangl2 is localised to junctions between IPhC and Pillar cells, and in the lateral sensory compartment, to the medial edge of OHC - DCs (Fig 4A). In KO, Vangl2 is enriched on junctions parallel to the medio-lateral axis in mKO cells. In lKO cells, this enrichment is much (Figure 4A). To understand that role of Vangl2 we analysed the *Vangl2*$^{Lp/Lp}$ mutant. This is a point mutation in Vangl2, and acts as a functional null . As has been described previously, at E18.5 we observed a decrease in the alignment of HC polarity for IHC and OHC (Figure 4B-D, Figure S11A-F) in homozygous (*Vangl2*$^{Lp/Lp}$) compared to their heterozygous (*Vangl2*$^{Lp/+}$) littermate controls [32] (Fig. 4B-D). In the medial sensory compartment, the decrease in alignment of planar polarity is accompanied with decrease in circularity and apical surface area of IHCs (Fig 4E, S11G). Similarly, in the lateral sensory compartment, the apical surface area and the circularity of OHCs is also decreased in

Vangl2$^{Lp/Lp}$ mutants (Fig 4F, S11H). The HCs in both medial and lateral sensory compartment showed a decrease in their row-wise organisation (Fig S11I-L). Despite this decrease in apical surface area and circularity of IHC and OHC, the width of the medial and lateral sensory compartments was comparable to the littermate heterozygous controls at the base and the middle turn of OC (Fig 4G, S11M N). At the apex, as previously described [32,33] we observed disorganised HCs leading to significant increase in the width of both medial and lateral sensory compartments (Fig S11B, M, N). Importantly, the proportion of vertices with 4 or more cells decreased significantly in the *Vangl2*$^{Lp/Lp}$ mutants, suggesting decreased cell intercalation (Fig. 4H). These data suggest that organisation of cells within medial and lateral sensory compartments is perturbed in the *Vangl2*$^{Lp/Lp}$ mutants.

We next analysed the KO compartment. The width of the KO domain is significantly narrower at the basal and the middle turn of the *Vangl2*$^{Lp/Lp}$ mutant OC (Figure 4I). Moreover, the difference in the apical surface area and the axis of elongation for cells in mKO and lKO was much reduced in *Vangl2*$^{Lp/Lp}$ (Figure 4J-L, S12). This reduction in difference between mKO and lKO cells is also observed in the proportion of vertices with 4 or more cells being significantly increased in the lateral KO and decreased in the medial KO in *Vangl2*$^{Lp/Lp}$ mutants (Fig 4H). The reduction in the differences of medial and lateral KO cells and the decrease in width of the KO compartments suggests that Vangl2 drives phenotypic characteristics of KO in addition to the medial and lateral sensory compartment.

Our data shows that looptail mutant of Vangl2 not only disrupts the organization of the medial and lateral sensory compartments of OC, it also disrupts the organisation of the KO. In both cases, this is likely through perturbations in cell rearrangements. This disruption is accompanied by defects in the shaping of each compartment. Within the constraints of the cochlear duct, the change in the shape of one compartment will affect others. Consistent with this is the change in cellular organisation at the apex of OC in looptail mutants, where

defective CE results in the accumulation of KO and medial and lateral sensory compartments. Here, the spatial organisation of the HC and SC of the sensory domains is perturbed. This suggests that the organisation within a compartment could influence the organisation within another. To investigate this, we used a compartment-specific deletion of Vangl2.

Compartment-intrinsic remodelling has extrinsic effects on cellular organisation

While looptail mutants show profound cochlear length and spiralling defects, an inner ear specific deletion of Vangl2 does not show defects in overall cochlea shape [58]. However, cellular organisation and HC polarity is nonetheless perturbed. To recapitulate this, we generated mice carrying one copy of the looptail mutation of Vangl2 and the other allele, the conditional Vangl2 flanked by loxP sites. We term this mouse *Vangl2*$^{lp/flox}$. Upon cre mediated recombination, the floxed allele is excised to generate *Vangl2*$^{lp/-}$ (See Fig. S13A and methods for details). We used *Sox10-Cre* which drives the expression in the inner ear as well as neural crest [59]. At E18.5, the length and width of the sensory region and KO compartment of the OC of the experimental animal (S*ox10cre*$^{+/-}$*:: Vangl2*$^{lp/-}$) was comparable to the littermate control cochlea (S*ox10cre*$^{-/-}$*:: Vangl2*$^{lp/flox}$*)* (Fig. S13B-D). This suggested a limited effect on CE of OC in this allele. However, both IHC and OHC in S*ox10cre*$^{+/-}$*:: Vangl2*$^{lp/-}$ mutants showed a reduction in the alignment of HC polarity (Fig. S13E-G) along with a decrease in circularity and the apical surface area (Fig. S13 H-K). In mutants (S*ox10cre*$^{+/-}$*:: Vangl2*$^{lp/-}$), the lKO cells no longer show a mediolateral orientation, although a difference in area is still observed (Fig. S13L-N).

We next used *Ngn1-457-Cre*, which drives expression in cells of the KO as well as the cochleo-vestibular ganglion, but is not active in the sensory region [60]. At E18.5, the cochlea from the experimental animal (*Ngn1-457-Cre*$^{+/-}$*:: Vangl2*$^{lp/-}$) showed a reduction in

difference of apical surface area between mKO and lKO cells compared to the littermate control (*Ngn1-457-Cre*$^{-/-}$*:: Vangl2*$^{lp/flox}$) cochlea (Fig. 5A, B). Similarly, the long axis of lKO cells in *Ngn1-457-Cre*$^{+/-}$*:: Vangl2*$^{lp/-}$ mutants was parallel to the OC tissue axis, compared to the orthogonal direction in the control cochlea (Fig. 5A, C). This suggests that a compartment-specific deletion of Vangl2 can result in a defect in local-scale cellular organisation. We assessed the cellular organisation in the sensory compartments to ask if these local, KO-specific perturbations affect other compartments. We did not observe significant defects in polarity, apical surface area or circularity in the medial sensory compartment (Fig. 5D, F). In contrast, while surface area and circularity were unaffected in the lateral sensory compartment, we noted a decreased alignment of planar polarity of OHC3 in *Ngn1-457-Cre*$^{+/-}$*:: Vangl2*$^{lp/-}$ mutants (Fig. 5D, E, G). This suggested that disruption of *Vangl2* from the non-sensory KO compartment could influence the development of planar polarity in the lateral sensory compartment (Fig. 5G). Previous work on the vestibular sensory epithelium [61], wing imaginal disc [62] and ommatidia[63], together with their mathematical description [64,65], suggests that a local deletion of PCP cues from a group of cells can also affect the polarity of neighbouring cells, a phenomenon known as domineering non-cell autonomy. In *Ngn1-457-Cre*$^{+/-}$*:: Vangl2*$^{lp/-}$ mutants, only the polarity of OHC3 cells are affected, which are at a considerable distance from the KO (Fig. 5H).

We next asked whether the sensory domain also influences the development of the non-sensory domain. To test this, we used *Lgr5-CreERT2*, a tamoxifen-inducible cre which, when induced at E15.5, drives recombination in the sensory domain but not in the KO. In the animals where recombination is induced at E15.5, we observed a reduction in planar polarity and circularity for HC at E18.5 (Fig. 6A-E). To ask if the KO is affected, we measured the apical surface area and the direction of the long axis in the lateral and medial KO. The mutant, tamoxifen-induced, KO compartment showed a slight decrease in the difference

between the apical surface area of the mKO and lKO cells (Fig. 6F, G). However, the mediolateral direction of the long axis of the lKO cells was abrogated (Fig. 6F, H). This data suggested a reciprocal influence of the sensory domain on cellular organisation within the KO compartment (Fig. 6I).

Taken together, our results show that compartments in the OC undergo compartment-specific cellular rearrangements and thereby adopt distinct morphologies. Importantly, our data suggests that compartments couple, with compartment-specific rearrangements influencing the cellular organisation in others. We thus asked the nature of compartment coupling in the OC.

Mechanical and Biochemical Origin of Coupling

Theoretical studies have suggested that an interaction between neighbouring domains may underlie the formation of hexatic order in the OHC domain [19]. Experimentally, we find a coupling between two distant compartments, the KO and the lateral sensory compartment. We reasoned that since a compartment-specific deletion of Vangl2 led to disruptions of cellular organisation at a distance, mechanistic insights of inter-domain coupling could be revealed by understanding the downstream signalling pathways of this gene. Vangl2 is known to modulate junctional activity, which underlies many cell behaviours [20,51-57]. Moreover, our work in the avian auditory epithelium suggested that Vangl2 regulates the di-phosphorylation of the regulatory light chain (RLC) of non-muscle myosin-2 (NMII) [20]. We thus investigated the patterns of p-RLC and pp-RLC in the OC.

At E18.5 p-RLC is expressed on all junctions (Fig. S14A). pp-RLC localization was similar to that of Vangl2; in the lateral sensory compartment, it was found at the medial edge of OHC-DC junctions (Fig. S14C, D). In the medial sensory compartment, pp-RLC was localised to IPhC-Pillar cells junctions (Fig. S14C, D), and in the KO compartment, it was

found along the junctions of the long-axis of KO cells (Figure S14B). In *Vangl2*$^{lp/lp}$ mutants, the localisation of p-RLC remained comparable to the littermate controls (Fig. S14E, F), however, pp-RLC was much reduced (Fig. S14G, H). These data suggest a role of Vangl2 in regulating pp-RLC activation and, thus, NMII activity (Figure S14 G, H). By using an organ culture method, we perturbed NMII activity using small molecule inhibitors of RLC phosphorylation. We cultured E16.5 explants for 8 hours, in the presence or absence of either ML7 (which inhibits Myosin Light Chain Kinase (MLCK)) or Y-27632 (which blocks Rho-associated Kinase (ROCK)) [66,67]. ROCK inhibition resulted in the abrogation of both p- and pp-RLC phosphorylation in the OC (Figure S15A-D). In such inhibited OC, we observed a decrease in alignment of HC polarity, apical surface area and circularity of OHC, compared to the control samples (Figure S15E-I). In addition, the differences in the apical surface area and the elongation axis of mKO and lKO cells was also reduced in the ROCK-inhibited OC (Figure S15E, J-L). In MLCK inhibited (ML7 25um) OC, the di-phosphorylated form of RLC is reduced (Figure S16A-D). In these explants, we observed a decrease in the alignment of HC polarity, circularity of HCs and the apical surface area for IHC (Figure S16E-I). The differences in apical surface area and the elongation axis of mKO and lKO cells were also reduced in the ML7-inhibited OC explants when compared to control samples (Figure S16J-L).

Our data showing that the Vangl2 phenotype can be recapitulated by inhibiting RLC phosphorylation suggests that junctional contractility underlies cellular organisation within compartments. We thus hypothesised that compartment coupling may depend on mechanics. Vinculin is critical for transmitting force between junctions (Fig. 7A) [68,69]. We reasoned that by removing this protein, the mechanical coupling between compartments would be impaired and result in defects in cellular organisation. We used a conditional allele of Vinculin (*Vinc*$^{fl/fl}$) and deleted this in the cochlea from E12.5 using Emx2-Cre. We could only obtain 3

experimental embryos out of 114 examined (see methods for detail). The OC from *Emx2-Cre*$^{+/-}$*::Vinc*$^{fl/fl}$ showed disruption in the alignment of planar polarity in the lateral sensory compartment (Figure 7B-F). In the KO, there is now a population of larger lKO cells abutting the medial sensory compartment (Fig 7B, G, H) in mutants. The differences in the direction of the long axis of lKO and mKO cells are reduced in *Emx2-Cre*$^{+/-}$*::Vinc*$^{fl/fl}$ (Fig. 7G, I). These data suggest the coupling between compartment is mediated, at least in part, through mechanics.

DISCUSSION

Using the mouse auditory epithelia we investigate a fundamental question in morphogenesis: How is development information organised such that tissues form shapes and patterns that are robust and reproducible? During the initial development of the cochlea duct, morphogen signalling establishes zones of defined by distinct complements of adhesion molecule expression, that resolve into compartments [12]. Compartments act as spatially restricted developmental units, each with distinct cell shapes and behaviours that drive distinct cellular organisation [1]. Using compartment-specific perturbations of cellular organisation, we find that these intra-compartment programmes show defects in the cellular organisation of other compartments. We consider this as evidence of inter-compartment coupling. Compartment coupling provides a mechanism that allows the transmission of morphogenetic information across spatial hierarchies, ensuring fidelity in organisation.

In addition to fine-graining positional information, developmental instructions should be organised in time. Compartment coupling is likely conditional upon the progression of intra-compartment cellular behaviours. Thus, it becomes possible that coupling could also temporally organise developmental instructions. This could include mechanical behaviours in adjacent domains, as is seen in the evagination of the chick feather bud placode or the

invagination of the hair follicles [70,71]. In the OC, we have identified mechanics via vinculin-mediated force transmission as coupling the KO compartment with a non-adjacent domain, the lateral sensory compartment. In all cases, the emergent behaviour that coupling controls is likely contingent on the intra-compartment behaviours.

The interfaces of compartments could also drive coupling through biochemical cues. The border between compartments establishes new sites of interaction that may lead to the formation new fates. This may be through the intersection of signals, as seen during the growth of Drosophila wings or leg discs [7,72]. Alternatively, the increased tension at the interfaces of compartments with different adhesion proteins may result in molecules expressing subsequent patterning information. In OC, the interface of Cdh2 expressing medial and Cdh1 expressing lateral sensory compartments acts as a secondary organiser. IHCs at this interface express Fgf8, which acts on neighbouring cells within the lateral sensory compartment to induce pillar cells [73]. Indeed, all compartment borders in the OC are interfaces between adhesion domains. These interfaces have unique cells (the inner border cells at the border between KO and the medial sensory compartment and outer border cells at the border between the later sensory and non-sensory compartments). Further investigation is required to ask whether the interfacial tension at these boundaries induces these cell types and whether they, too, can act as secondary organisers. The lateral KO cells are noteworthy. They are larger and have shifted their long axis perpendicularly to medial KO cells. As they abut the medial sensory compartment, it is tempting to speculate that this reconfiguration results from compartment coupling. However, we note that the appearance of lKO cells is perturbed in *Vangl2*$^{lp/lp}$ mutants but not in the inner ear-specific S*ox10cre*$^{+/-}$*:: Vangl2*$^{lp/-}$. This suggests an influence of Vangl2, extrinsic to the inner ear, which plays a role in lKO specialisation.

Our data identifies compartments as a mechanism that permits distinct patterns of cellular organisation within an organ. Compartments bridge scales between embryonic fields

and cells. Coupling between compartments also provides a mechanism for the temporal organisation of this information. We suggest that compartments and their coupling provide a conceptual framework to spatially and temporally organise morphogenetic information that is relevant not only to the development of the inner ear but, more generally, during organogenesis.

ACKNOWLEDGEMENTS

This work was supported by the Department of Atomic Energy, Government of India, Project Identification No. RTI 4006, and grants from SERB, TIFR Infosys-Leading Edge Grant, the Royal National Institute for Deaf People, and the International Foundation for Research and Education, via a Simons-Ashoka ECF fellowship to AP, for this research. We thank Central Imaging and Flowcytometry Facility (CIFF), Animal Care and Resource Centre (ACRC) and laboratory kitchen at NCBS. We thank Srikala Raghvan for providing the Vinculin mouse. We thank Sandeep Krishna for inputs on quantifying the row-wise arrangement of HCs. We thank Hiroshi Hamada and Sandeep Krishna for comments on the manuscript. A. P. thanks ICTP - ICTS Winter School on Quantitative Systems Biology for introducing quantitative morphogenesis. The Myo7a antibody developed by Dana J. Orten, E-cadherin antibody developed by Warren Gallin, and the N-cadherin antibody developed by Karen A Knudsen was obtained from the Developmental Studies Hybridoma Bank, created by the NICHD of the NIH and maintained at The University of Iowa, Department of Biology, Iowa City, IA 52242. Cdkn1b antibody was a kind gift from Dr Dimple Notani. We are grateful to members of Ear Lab for feedback.

AUTHOUR CONTRIBUTIONS

A.P. and R.K.L conceived the project and designed the experiments. A.P performed experiments and analysed the data. A.P. and S.R. performed Vangl2 lgr5 experiments. S.R. and R.K helped in generating different mouse strains and provided inputs in experimental design and manuscript preparation. A.S.I and A.P. developed codes to analyse data. A.P. and R.K.L wrote and revised the manuscript.

DECLARATION OF CONFLICTS OF INTEREST

All authors declare no conflicts of interest

DATA AND CODE AVAILABILITY

Codes related to this work would be submitted on GitHub after acceptance of the manuscript. All raw data would be available upon request.

REFERENCES

1. Morata, G., and Lawrence, P. (2022). An exciting period of Drosophila developmental biology: Of imaginal discs, clones, compartments, parasegments and homeotic genes. Dev Biol *484*, 12-21. 10.1016/j.ydbio.2022.01.008.
2. McGuigan, A.P., and Javaherian, S. (2016). Tissue Patterning: Translating Design Principles from In Vivo to In Vitro. Annu Rev Biomed Eng *18*, 1-24. 10.1146/annurev-bioeng-083115-032943.
3. Wang, J., and Dahmann, C. (2020). Establishing compartment boundaries in Drosophila wing imaginal discs: An interplay between selector genes, signaling pathways and cell mechanics. Semin Cell Dev Biol *107*, 161-169. 10.1016/j.semcdb.2020.07.008.
4. Sharrock, T.E., and Sanson, B. (2020). Cell sorting and morphogenesis in early Drosophila embryos. Semin Cell Dev Biol *107*, 147-160. 10.1016/j.semcdb.2020.07.010.
5. Sela-Donenfeld, D., Kayam, G., and Wilkinson, D.G. (2009). Boundary cells regulate a switch in the expression of FGF3 in hindbrain rhombomeres. BMC Dev Biol *9*, 16. 10.1186/1471-213X-9-16.
6. Irvine, K.D., and Wieschaus, E. (1994). fringe, a Boundary-specific signaling molecule, mediates interactions between dorsal and ventral cells during Drosophila wing development. Cell *79*, 595-606. 10.1016/0092-8674(94)90545-2.
7. Vincent, J.P., and Lawrence, P.A. (1994). Drosophila wingless sustains engrailed expression only in adjoining cells: evidence from mosaic embryos. Cell *77*, 909-915. 10.1016/0092-8674(94)90139-2.
8. Basch, M.L., Brown, R.M., 2nd, Jen, H.I., and Groves, A.K. (2016). Where hearing starts: the development of the mammalian cochlea. J Anat *228*, 233-254. 10.1111/joa.12314.
9. Wu, D.K., and Kelley, M.W. (2012). Molecular mechanisms of inner ear development. Cold Spring Harbor perspectives in biology *4*, a008409. 10.1101/cshperspect.a008409.
10. Cohen, R., and Sprinzak, D. (2021). Mechanical forces shaping the development of the inner ear. Biophys J *120*, 4142-4148. 10.1016/j.bpj.2021.06.036.
11. Vater, M., and Kossl, M. (2011). Comparative aspects of cochlear functional organization in mammals. Hear Res *273*, 89-99. 10.1016/j.heares.2010.05.018.
12. Munnamalai, V., and Fekete, D.M. (2020). The acquisition of positional information across the radial axis of the cochlea. Dev Dyn *249*, 281-297. 10.1002/dvdy.118.
13. Groves, A.K., and Fekete, D.M. (2012). Shaping sound in space: the regulation of inner ear patterning. Development *139*, 245-257.
14. Chen, P., and Segil, N. (1999). p27(Kip1) links cell proliferation to morphogenesis in the developing organ of Corti. Development *126*, 1581-1590.
15. Lanford, P.J., Lan, Y., Jiang, R., Lindsell, C., Weinmaster, G., Gridley, T., and Kelley, M.W. (1999). Notch signalling pathway mediates hair cell development in mammalian cochlea. Nat Genet *21*, 289-292.

16. Jacobo, A., Dasgupta, A., Erzberger, A., Siletti, K., and Hudspeth, A.J. (2019). Notch-Mediated Determination of Hair-Bundle Polarity in Mechanosensory Hair Cells of the Zebrafish Lateral Line. Curr Biol *29*, 3579-3587 e3577. 10.1016/j.cub.2019.08.060.
17. Togashi, H., Kominami, K., Waseda, M., Komura, H., Miyoshi, J., Takeichi, M., and Takai, Y. (2011). Nectins establish a checkerboard-like cellular pattern in the auditory epithelium. Science *333*, 1144-1147. 10.1126/science.1208467.
18. Fukuda, T., Kominami, K., Wang, S., Togashi, H., Hirata, K., Mizoguchi, A., Rikitake, Y., and Takai, Y. (2014). Aberrant cochlear hair cell attachments caused by Nectin-3 deficiency result in hair bundle abnormalities. Development *141*, 399-409. 10.1242/dev.094995.
19. Cohen, R., Amir-Zilberstein, L., Hersch, M., Woland, S., Loza, O., Taiber, S., Matsuzaki, F., Bergmann, S., Avraham, K.B., and Sprinzak, D. (2020). Mechanical forces drive ordered patterning of hair cells in the mammalian inner ear. Nature communications *11*, 5137. 10.1038/s41467-020-18894-8.
20. Prakash, A., Weninger, J., Singh, N., Raman, S., Kruse, K., Rao, M., and Ladher, R.K. (2023). Junctional Force Patterning drives both Positional and Orientational Order in Auditory Epithelia. 10.21203/rs.3.rs-2508957/v1.
21. Yamamoto, N., Okano, T., Ma, X., Adelstein, R.S., and Kelley, M.W. (2009). Myosin II regulates extension, growth and patterning in the mammalian cochlear duct. Development *136*, 1977-1986. 10.1242/dev.030718.
22. Driver, E.C., Northrop, A., and Kelley, M.W. (2017). Cell migration, intercalation and growth regulate mammalian cochlear extension. Development *144*, 3766-3776. 10.1242/dev.151761.
23. Chacon-Heszele, M.F., Ren, D., Reynolds, A.B., Chi, F., and Chen, P. (2012). Regulation of cochlear convergent extension by the vertebrate planar cell polarity pathway is dependent on p120-catenin. Development *139*, 968-978. 10.1242/dev.065326.
24. Wang, J., Mark, S., Zhang, X., Qian, D., Yoo, S.J., Radde-Gallwitz, K., Zhang, Y., Lin, X., Collazo, A., Wynshaw-Boris, A., and Chen, P. (2005). Regulation of polarized extension and planar cell polarity in the cochlea by the vertebrate PCP pathway. Nat Genet *37*, 980-985.
25. Ishii, M., Tateya, T., Matsuda, M., and Hirashima, T. (2021). Stalling interkinetic nuclear migration in curved pseudostratified epithelium of developing cochlea. R Soc Open Sci *8*, 211024. 10.1098/rsos.211024.
26. Ishii, M., Tateya, T., Matsuda, M., and Hirashima, T. (2021). Retrograde ERK activation waves drive base-to-apex multicellular flow in murine cochlear duct morphogenesis. eLife *10*. 10.7554/eLife.61092.
27. McKenzie, E., Krupin, A., and Kelley, M.W. (2004). Cellular growth and rearrangement during the development of the mammalian organ of Corti. Dev Dyn *229*, 802-812. 10.1002/dvdy.10500.
28. Kelley, M.W. (2007). Cellular commitment and differentiation in the organ of Corti. Int J Dev Biol *51*, 571-583. 10.1387/ijdb.072388mk.

29. Sano, H., Mukai, J., Monoo, K., Close, L.G., and Sato, T.A. (2001). Expression of p75NTR and its associated protein NADE in the rat cochlea. Laryngoscope *111*, 535-538. 10.1097/00005537-200103000-00027.
30. Saino-Saito, S., Suzuki, R., Tokuda, N., Abe, H., Kondo, H., and Owada, Y. (2010). Localization of fatty acid binding proteins (FABPs) in the cochlea of mice. Ann Anat *192*, 210-214. 10.1016/j.aanat.2010.06.007.
31. Basch, M.L., Brown, R.M., 2nd, Jen, H.I., Semerci, F., Depreux, F., Edlund, R.K., Zhang, H., Norton, C.R., Gridley, T., Cole, S.E., et al. (2016). Fine-tuning of Notch signaling sets the boundary of the organ of Corti and establishes sensory cell fates. eLife *5*. 10.7554/eLife.19921.
32. Montcouquiol, M., Rachel, R.A., Lanford, P.J., Copeland, N.G., Jenkins, N.A., and Kelley, M.W. (2003). Identification of Vangl2 and Scrb1 as planar polarity genes in mammals. Nature *423*, 173-177.
33. Montcouquiol, M., Sans, N., Huss, D., Kach, J., Dickman, J.D., Forge, A., Rachel, R.A., Copeland, N.G., Jenkins, N.A., Bogani, D., et al. (2006). Asymmetric localization of Vangl2 and Fz3 indicate novel mechanisms for planar cell polarity in mammals. J Neurosci *26*, 5265-5275.
34. Yang, W., Garrett, L., Feng, D., Elliott, G., Liu, X., Wang, N., Wong, Y.M., Choi, N.T., Yang, Y., and Gao, B. (2017). Wnt-induced Vangl2 phosphorylation is dose-dependently required for planar cell polarity in mammalian development. Cell Res *27*, 1466-1484. 10.1038/cr.2017.127.
35. Yin, H., Copley, C.O., Goodrich, L.V., and Deans, M.R. (2012). Comparison of phenotypes between different vangl2 mutants demonstrates dominant effects of the Looptail mutation during hair cell development. PLoS One *7*, e31988. 10.1371/journal.pone.0031988.
36. Tsai, T.Y., Sikora, M., Xia, P., Colak-Champollion, T., Knaut, H., Heisenberg, C.P., and Megason, S.G. (2020). An adhesion code ensures robust pattern formation during tissue morphogenesis. Science *370*, 113-116. 10.1126/science.aba6637.
37. Takeichi, M., Atsumi, T., Yoshida, C., Uno, K., and Okada, T.S. (1981). Selective adhesion of embryonal carcinoma cells and differentiated cells by Ca2+-dependent sites. Dev Biol *87*, 340-350. 10.1016/0012-1606(81)90157-3.
38. Foty, R.A., and Steinberg, M.S. (2013). Differential adhesion in model systems. Wiley interdisciplinary reviews. Developmental biology *2*, 631-645. 10.1002/wdev.104.
39. Duguay, D., Foty, R.A., and Steinberg, M.S. (2003). Cadherin-mediated cell adhesion and tissue segregation: qualitative and quantitative determinants. Dev Biol *253*, 309-323. 10.1016/s0012-1606(02)00016-7.
40. Simonneau, L., Gallego, M., and Pujol, R. (2003). Comparative expression patterns of T-, N-, E-cadherins, beta-catenin, and polysialic acid neural cell adhesion molecule in rat cochlea during development: implications for the nature of Kolliker's organ. J Comp Neurol *459*, 113-126. 10.1002/cne.10604.
41. Maunsell, H.R., Ellis, K., Kelley, M.W., and Driver, E.C. (2023). Lrrn1 Regulates Medial Boundary Formation in the Developing Mouse Organ of Corti. J Neurosci *43*, 5305-5318. 10.1523/JNEUROSCI.2141-22.2023.

42. Choi, Y.S., and Gumbiner, B. (1989). Expression of cell adhesion molecule E-cadherin in Xenopus embryos begins at gastrulation and predominates in the ectoderm. J Cell Biol *108*, 2449-2458. 10.1083/jcb.108.6.2449.
43. George-Weinstein, M., Gerhart, J., Blitz, J., Simak, E., and Knudsen, K.A. (1997). N-cadherin promotes the commitment and differentiation of skeletal muscle precursor cells. Dev Biol *185*, 14-24. 10.1006/dbio.1997.8542.
44. Umetsu, D., Aigouy, B., Aliee, M., Sui, L., Eaton, S., Julicher, F., and Dahmann, C. (2014). Local increases in mechanical tension shape compartment boundaries by biasing cell intercalations. Curr Biol *24*, 1798-1805. 10.1016/j.cub.2014.06.052.
45. Huh, S.H., Jones, J., Warchol, M.E., and Ornitz, D.M. (2011). Differentiation of the lateral compartment of the cochlea requires a temporally restricted FGF20 signal. PLoS Biol *10*, e1001231.
46. Ono, K., Kita, T., Sato, S., O'Neill, P., Mak, S.S., Paschaki, M., Ito, M., Gotoh, N., Kawakami, K., Sasai, Y., and Ladher, R.K. (2014). FGFR1-Frs2/3 signalling maintains sensory progenitors during inner ear hair cell formation. PLoS Genet *10*, e1004118. 10.1371/journal.pgen.1004118.
47. Pirvola, U., Ylikoski, J., Trokovic, R., Hebert, J.M., McConnell, S.K., and Partanen, J. (2002). FGFR1 is required for the development of the auditory sensory epithelium. Neuron *35*, 671-680.
48. Hayashi, T., Ray, C.A., and Bermingham-McDonogh, O. (2008). Fgf20 is required for sensory epithelial specification in the developing cochlea. J Neurosci *28*, 5991-5999.
49. Pujades, C. (2020). The multiple functions of hindbrain boundary cells: Tinkering boundaries? Semin Cell Dev Biol *107*, 179-189. 10.1016/j.semcdb.2020.05.002.
50. Chakravarthy, S.R., van Zanten, T.S., and Ladher, R.K. (2024). Initiation and Formation of Stereocilia during the Development of Mouse Cochlear Hair Cells. bioRxiv, 2024.2003.2023.586377. 10.1101/2024.03.23.586377.
51. Vichas, A., and Zallen, J.A. (2011). Translating cell polarity into tissue elongation. Semin Cell Dev Biol *22*, 858-864. 10.1016/j.semcdb.2011.09.013.
52. Winter, C.G., Wang, B., Ballew, A., Royou, A., Karess, R., Axelrod, J.D., and Luo, L. (2001). Drosophila Rho-associated kinase (Drok) links Frizzled-mediated planar cell polarity signaling to the actin cytoskeleton. Cell *105*, 81-91. 10.1016/s0092-8674(01)00298-7.
53. Dawes-Hoang, R.E., Parmar, K.M., Christiansen, A.E., Phelps, C.B., Brand, A.H., and Wieschaus, E.F. (2005). folded gastrulation, cell shape change and the control of myosin localization. Development *132*, 4165-4178.
54. Simoes Sde, M., Mainieri, A., and Zallen, J.A. (2014). Rho GTPase and Shroom direct planar polarized actomyosin contractility during convergent extension. J Cell Biol *204*, 575-589. 10.1083/jcb.201307070.
55. Newman-Smith, E., Kourakis, M.J., Reeves, W., Veeman, M., and Smith, W.C. (2015). Reciprocal and dynamic polarization of planar cell polarity core components and myosin. eLife *4*, e05361. 10.7554/eLife.05361.

56. Shindo, A., and Wallingford, J.B. (2014). PCP and septins compartmentalize cortical actomyosin to direct collective cell movement. Science *343*, 649-652. 10.1126/science.1243126.
57. Nishimura, T., Honda, H., and Takeichi, M. (2012). Planar cell polarity links axes of spatial dynamics in neural-tube closure. Cell *149*, 1084-1097. 10.1016/j.cell.2012.04.021.
58. Copley, C.O., Duncan, J.S., Liu, C., Cheng, H., and Deans, M.R. (2013). Postnatal refinement of auditory hair cell planar polarity deficits occurs in the absence of Vangl2. J Neurosci *33*, 14001-14016. 10.1523/JNEUROSCI.1307-13.2013.
59. Matsuoka, T., Ahlberg, P.E., Kessaris, N., Iannarelli, P., Dennehy, U., Richardson, W.D., McMahon, A.P., and Koentges, G. (2005). Neural crest origins of the neck and shoulder. Nature *436*, 347-355. 10.1038/nature03837.
60. Quinones, H.I., Savage, T.K., Battiste, J., and Johnson, J.E. (2010). Neurogenin 1 (Neurog1) expression in the ventral neural tube is mediated by a distinct enhancer and preferentially marks ventral interneuron lineages. Dev Biol *340*, 283-292. 10.1016/j.ydbio.2010.02.012.
61. Stoller, M.L., Roman, O., Jr., and Deans, M.R. (2018). Domineering non-autonomy in Vangl1;Vangl2 double mutants demonstrates intercellular PCP signaling in the vertebrate inner ear. Dev Biol *437*, 17-26. 10.1016/j.ydbio.2018.02.021.
62. Adler, P.N., Taylor, J., and Charlton, J. (2000). The domineering non-autonomy of frizzled and van Gogh clones in the Drosophila wing is a consequence of a disruption in local signaling. Mech Dev *96*, 197-207. 10.1016/s0925-4773(00)00392-0.
63. Strutt, H., and Strutt, D. (2002). Nonautonomous planar polarity patterning in Drosophila: dishevelled-independent functions of frizzled. Dev Cell *3*, 851-863. 10.1016/s1534-5807(02)00363-5.
64. Amonlirdviman, K., Khare, N.A., Tree, D.R., Chen, W.S., Axelrod, J.D., and Tomlin, C.J. (2005). Mathematical modeling of planar cell polarity to understand domineering nonautonomy. Science *307*, 423-426. 10.1126/science.1105471.
65. Zhu, H. (2009). Is anisotropic propagation of polarized molecular distribution the common mechanism of swirling patterns of planar cell polarization? Journal of theoretical biology *256*, 315-325. 10.1016/j.jtbi.2008.08.029.
66. Uehata, M., Ishizaki, T., Satoh, H., Ono, T., Kawahara, T., Morishita, T., Tamakawa, H., Yamagami, K., Inui, J., Maekawa, M., and Narumiya, S. (1997). Calcium sensitization of smooth muscle mediated by a Rho-associated protein kinase in hypertension. Nature *389*, 990-994. 10.1038/40187.
67. Saitoh, M., Ishikawa, T., Matsushima, S., Naka, M., and Hidaka, H. (1987). Selective inhibition of catalytic activity of smooth muscle myosin light chain kinase. J Biol Chem *262*, 7796-7801.
68. Yonemura, S., Wada, Y., Watanabe, T., Nagafuchi, A., and Shibata, M. (2010). alpha-Catenin as a tension transducer that induces adherens junction development. Nat Cell Biol *12*, 533-542. 10.1038/ncb2055.
69. Biswas, R., Banerjee, A., Lembo, S., Zhao, Z., Lakshmanan, V., Lim, R., Le, S., Nakasaki, M., Kutyavin, V., Wright, G., et al. (2021). Mechanical instability of

adherens junctions overrides intrinsic quiescence of hair follicle stem cells. Dev Cell *56*, 761-780 e767. 10.1016/j.devcel.2021.02.020.

70. Yang, S., Palmquist, K.H., Nathan, L., Pfeifer, C.R., Schultheiss, P.J., Sharma, A., Kam, L.C., Miller, P.W., Shyer, A.E., and Rodrigues, A.R. (2023). Morphogens enable interacting supracellular phases that generate organ architecture. Science *382*, eadg5579. 10.1126/science.adg5579.
71. Villeneuve, C., Hashmi, A., Ylivinkka, I., Lawson-Keister, E., Miroshnikova, Y.A., Perez-Gonzalez, C., Myllymaki, S.M., Bertillot, F., Yadav, B., Zhang, T., et al. (2024). Mechanical forces across compartments coordinate cell shape and fate transitions to generate tissue architecture. Nat Cell Biol *26*, 207-218. 10.1038/s41556-023-01332-4.
72. Lecuit, T., Brook, W.J., Ng, M., Calleja, M., Sun, H., and Cohen, S.M. (1996). Two distinct mechanisms for long-range patterning by Decapentaplegic in the Drosophila wing. Nature *381*, 387-393. 10.1038/381387a0.
73. Jacques, B.E., Montcouquiol, M.E., Layman, E.M., Lewandoski, M., and Kelley, M.W. (2007). Fgf8 induces pillar cell fate and regulates cellular patterning in the mammalian cochlea. Development *134*, 3021-3029.

FIGURE LEGENDS

Figure 1. Cellular organisation is preserved in looptail mutants with defective convergent extension.

A. Schematic of spiral-shaped mouse organ of Corti (OC) representing KÖlliker's organ (medial non-sensory domain), sensory domain and lateral non-sensory domain.
B. OC from embryonic day (E)18.5 heterozygous (*Vangl2* $^{Lp/+}$) and homozygous (*Vangl2* $^{Lp/Lp}$) looptail mutant stained for f-actin (green).
C. Length of E18.5 cochlea from heterozygous (*Vangl2* $^{Lp/+}$) and homozygous (*Vangl2* $^{Lp/Lp}$) looptail mutant. N=4 / 5 (Het/Homo)
D. Base of E18.5 OC from heterozygous (*Vangl2* $^{Lp/+}$) and homozygous (*Vangl2* $^{Lp/Lp}$) looptail mutant stained for F-actin (green) and Myosin 7a (magenta and grey). N= 4.
E. Base of E18.5 OC from heterozygous (*Vangl2* $^{Lp/+}$) and homozygous (*Vangl2* $^{Lp/Lp}$) looptail mutant stained for F-actin (green) and BLBP (magenta and grey). N= 4.
F. Base of E18.5 OC from heterozygous (*Vangl2* $^{Lp/+}$) and homozygous (*Vangl2* $^{Lp/Lp}$) looptail mutant stained for F-actin (green) and p75NTR (magenta and grey). N= 4.
G. Base of E18.5 OC from heterozygous (*Vangl2* $^{Lp/+}$) and homozygous (*Vangl2* $^{Lp/Lp}$) looptail mutant stained for F-actin (grey). Asterisks indicates Hensen's (magenta) and Claudius' (cyan) cells of the lateral non-sensory domain, and arrowheads indicates Kölliker's organ. N=8
H. Schematic representing the preservation of cellular organisation along the medio-lateral axis in OC.

Unpaired T-test.
Scale Bar: 5µm and 50µm in B.
Image orientation: Top is lateral, Right is Apex.

Figure 2. Adhesion-code preserves the cellular organisation during convergent extension mediated extension of OC.

A. E18.5 OC stained for F-actin (green) and Nectin2 (magenta and grey).
B. E18.5 OC stained for F-actin (green) and Cdh1 (magenta and grey).
C. E18.5 OC stained for F-actin (green) and Cdh2 (magenta and grey).
D. E18.5 OC stained for F-actin (green) and Cdh4 (magenta and grey).
E. Schematic representing the collagen droplet culture.
F. Schematic representing the Cadherin blocking experiments done ex-vivo.
G. 12-hour explant of E15.5 OC in presence of Bovine Serum Albumin (BSA, 0.1%) stained for F-actin (green) and Arl13b (magenta). N=4 cochlea
H. 12-hour explant of E15.5 OC in presence of Bovine Serum Albumin (BSA, 0.1%) stained for F-actin (green) and p75NTR (magenta). Insets represent p75NTR expression in grey and schematic of cellular organisation. N=4 cochlea. Scale Bar: 5µm
I. 12-hour explant of E15.5 OC in presence of Cdh1 blocking antibodies (7D6, 10ug/ml) stained for F-actin (green) and Arl13b (magenta). Arrowheads represents the interface between Hensen's cells and Outer HCs. N=4 cochlea.

J. 12-hour explant of E15.5 OC in presence of Cdh1 blocking antibodies (7D6, 10ug/ml) stained for F-actin (green) and p75NTR (magenta). Arrowheads indicates the interface between Hensen's cells and Outer HCs. Insets represent p75NTR expression in grey and schematic of cellular organisation. N=4 cochlea.
K. 12-hour explant of E15.5 OC in presence of Cdh2 blocking antibodies (6B3, 10ug/ml) stained for F-actin (green) and Arl13b (magenta). Arrowheads represents the disorganisation of Inner HCs. N=4 cochlea.
L. 12-hour explant of E15.5 OC in presence of Cdh2 blocking antibodies (6B3, 10ug/ml) stained for F-actin (green) and p75NTR (magenta). Arrowheads represents the disorganisation of Inner Phalangeal cells. Insets represent p75NTR expression in grey and schematic of cellular organisation. N=4 cochlea.

Scale Bar: 10µm in A-D, 5µm in G-L.
Image orientation: Top is lateral, Right is Apex.

Figure 3. Sensory and non-sensory domain acquires discrete ordering.

A. Base region (30P) of OC from E15.5, E16.5 and E18.5 stained for F-actin (green) and Arl13b (magenta).
B. Width of the sensory domain along the OC at E15.5 and E18.5. N=4 cochlea for each stage.
C. Width of the KÖlliker's organ along the OC at E15.5 and E18.5. N=4 cochlea for each stage.
D. Base region (30P) of OC from E15.5 and E18.5 stained for F-actin (grey).
E. Schematic representing the medial KÖlliker's organ (mKO) and lateral KÖlliker's organ (lKO).
F. Apical surface area of mKO and lKO at E15.5 and E18.5 at basal region (30P). N= 378/303 (mKO/lKO, E15.5) and 283/298 (mKO/lKO, E18.5); 4 cochlea each stage.
G. Rose stack plot representing the axis of elongation cells at mKO and lKO at E15.5 and E18.5. N= 378/303 (mKO/lKO, E15.5) and 283/298 (mKO/lKO, E18.5); 4 cochlea each stage.

Scale Bar: 10µm
Unpaired T-test, * =P<0.05, **=P<0.01
Image orientation: Top is lateral, Right is Apex.

Figure 4. Looptail mutant disrupts organisation in each compartment.

A. E18.5 OC stained for F-actin (green) and Vangl2 (magenta).
B. Base region (30P) of E18.5 OC from heterozygous (*Vangl2* $^{Lp/+}$) and homozygous (*Vangl2* $^{Lp/Lp}$) looptail mutant stained for F-actin (green) and Arl13b (magenta). N= 6 cochlea.
C. Polar coordinates of kinocilia of IHC at Base region (30P) of E18.5 OC from heterozygous (*Vangl2* $^{Lp/+}$) in orange and homozygous (*Vangl2* $^{Lp/Lp}$) looptail mutant in blue. N=66/66 (Het/Homo)

D. Polar coordinates of kinocilia of OHC at Base region (30P) of E18.5 OC from heterozygous (*Vangl2* $^{Lp/+}$) in orange and homozygous (*Vangl2* $^{Lp/Lp}$) looptail mutant in blue. N=110/110 (Het/Homo)
E. Circularity of IHC from heterozygous (*Vangl2* $^{Lp/+}$) and homozygous (*Vangl2* $^{Lp/Lp}$) looptail mutant at E18.5. N=210/219 (Het/Homo)
F. Circularity of OHC from heterozygous (*Vangl2* $^{Lp/+}$) and homozygous (*Vangl2* $^{Lp/Lp}$) looptail mutant at E18.5. N= 345/359 (Het/Homo)
G. Width of sensory domain along the OC form heterozygous (*Vangl2* $^{Lp/+}$) and homozygous (*Vangl2* $^{Lp/Lp}$) looptail mutant at E18.5. N=4 each
H. Percentage of vertices with 4 or more cells for mKO, lKO and sensory domain in OC from heterozygous (*Vangl2* $^{Lp/+}$) and homozygous (*Vangl2* $^{Lp/Lp}$) looptail mutant at E18.5. N= 3 cochlea each, 250/622 mKO; 113/923 lKO; 155/880 sensory in Het and 249/921 mKO; 261/1215 lKO; 131/1079 sensory in Homo. (4 or more cell vertices /Total vertices)
I. Width of KÖlliker's organ along the OC from heterozygous (*Vangl2* $^{Lp/+}$) and homozygous (*Vangl2* $^{Lp/Lp}$) looptail mutant at E18.5. N=4 embryos.
J. Base region (30P) of E18.5 OC from heterozygous (*Vangl2* $^{Lp/+}$) and homozygous (*Vangl2* $^{Lp/Lp}$) looptail mutant stained for F-actin (grey).
K. Rose stack plot representing the axis of cell elongation for mKO and lKO cells at the base region (30P) of E18.5 OC from heterozygous (*Vangl2* $^{Lp/+}$) and homozygous (*Vangl2* $^{Lp/Lp}$) looptail mutant. N=218/224 (mKO/lKO, Het) and 234/198 (mKO/lKO, Homo).
L. Apical surface area of mKO and lKO cells at Base region (30P) of E18.5 OC from heterozygous (*Vangl2* $^{Lp/+}$) and homozygous (*Vangl2* $^{Lp/Lp}$) looptail mutant. N=218/224 (mKO/lKO, Het) and 234/198 (mKO/lKO, Homo).

Scale Bar: 5µm in A, B and 10µm in J
Unpaired T-test, * =P<0.05, **=P<0.01
Image orientation: Top is lateral, Right is Apex.

Figure 5. Deletion of Vangl2 from KÖlliker's organ disrupts organisation in lateral sensory domain.

A. KÖlliker's organ from base region (30P) of OC from Cre negative control (*Ngn1-457-Cre*$^{+/+-}$*:: Vangl2*$^{lp/fl}$) and Ngn1-457cre positive mutant (*Ngn1-457-Cre*$^{+/-}$*:: Vangl2*$^{lp/fl}$) stained for F-actin (grey). N=4 embryos.
B. Apical surface area of medial and lateral KO cells from Cre negative control (*Ngn1-457-Cre*$^{+/+-}$*:: Vangl2*$^{lp/fl}$) and Ngn1-457cre positive mutant (*Ngn1-457-Cre*$^{+/-}$*:: Vangl2*$^{lp/fl}$) OC. N= 190/202 for Control and 198/208 for Mutant (mKO/lKO).
C. Rose stack plots representing the axis of cell elongation in medial and lateral KO cells from Cre negative control (*Ngn1-457-Cre*$^{+/+-}$*:: Vangl2*$^{lp/fl}$) and Ngn1-457cre positive mutant (*Ngn1-457-Cre*$^{+/-}$*:: Vangl2*$^{lp/fl}$) OC. N= 190/202 for Control and 198/208 for Mutant (mKO/lKO).

D. Base region (30P) of OC from Cre negative control (*Ngn1-457-Cre*$^{+/+-}$*:: Vangl2*$^{lp/fl}$) and Ngn1-457cre positive mutant (*Ngn1-457-Cre*$^{+/-}$*:: Vangl2*$^{lp/fl}$) stained for F-actin (green) and Arl13b (magenta).
E. Polar coordinates representing the position of kinocilia from IHC and OHC of Cre negative control (*Ngn1-457-Cre*$^{+/+-}$*:: Vangl2*$^{lp/fl}$) in orange and Ngn1-457cre positive mutant (*Ngn1-457-Cre*$^{+/-}$*:: Vangl2*$^{lp/fl}$) in blue. N= 66/66 for IHC and N= 113/121 for OHC (control/mutant).
F. Apical surface area and Circularity of IHC of Cre negative control (*Ngn1-457-Cre*$^{+/+-}$ *:: Vangl2*$^{lp/fl}$) in orange and Ngn1-457cre positive mutant (*Ngn1-457-Cre*$^{+/-}$*:: Vangl2*$^{lp/fl}$) in blue. N=92/96 (control/mutant).
G. Apical surface area and Circularity of OHC of Cre negative control (*Ngn1-457-Cre*$^{+/+-}$*:: Vangl2*$^{lp/fl}$) in orange and Ngn1-457cre positive mutant (*Ngn1-457-Cre*$^{+/-}$*:: Vangl2*$^{lp/fl}$) in blue. N= 143/151 (control/mutant).
H. Schematic representing the expression of cre in KO compartment (magenta), hence the deletion of Vangl2 from the KO and the effect on the organisation in lateral sensory compartment (green).

Scale Bar: 10 µm in A and 5µm in D
Unpaired T-test, ns=P>0.05, non-significant.
Ngn1-457 Cre$^{+/+}$ means cre negative and Ngn1-457 Cre$^{+/-}$ means cre positive
Image orientation: Top is lateral, Right is Apex.

Figure 6. Deletion of Vangl2 from sensory compartments disrupts organisation in KO compartment.

A. Base region (30P) of OC from corn oil injected control (*Lgr5CreERT2*$^{+/-}$*:: Vangl2*$^{lp/fl}$*::Corn oil*) and tamoxifen induced mutant (*Lgr5CreERT2*$^{+/-}$*:: Vangl2*$^{lp/fl}$*::Corn oil*) stained for F-actin (green) and Arl13b (magenta).
B. Polar coordinates representing the position of kinocilia of IHC from corn oil injected control OC in orange and tamoxifen-induced mutant in blue. N= 66/66 (corn oil/Tamoxifen).
C. Polar coordinates representing the position of kinocilia of OHC from corn oil injected control OC in orange and tamoxifen-induced mutant in blue. N=110/110 (Corn oil/Tamoxifen)
D. Apical surface area and Circularity of IHC from corn oil injected control OC in orange and tamoxifen-induced mutant in blue. N= 89/99 (corn oil/Tamoxifen)
E. Apical surface area and circularity of OHC from corn oil injected control OC in orange and tamoxifen-induced mutant in blue. N= 109/128 (corn oil/Tamoxifen)
F. KÖlliker's organ from base region (30P) of OC from corn oil injected control OC and tamoxifen-induced mutant embryos stained for F-actin(grey). Scale Bar: 10µm
G. Apical surface area of medial and lateral KO cells from corn oil injected control and tamoxifen-induced mutant OC. N=265/245 for Corn oil and 264/234 for Tamoxifen (mKO/lKO).

H. Rose stack plots representing the axis of cell elongation in medial and lateral KO cells from corn oil injected control and tamoxifen induced mutant OC. N=265/245 for Corn oil and 264/234 for Tamoxifen (mKO/lKO).
I. Schematic representing the expression of cre in lateral and medial sensory compartments (magenta) and hence the deletion of Vangl2, with the effect on the organisation in the KO (green).

Scale Bar: 5 µm in A and 10 µm in F
Unpaired T-test.
Image orientation: Top is lateral, Right is Apex.

Figure 7. Disruption of Junctional force transmission complex protein, Vinculin, disrupts the organisation of OC.

A. Schematic representing the communication between cells of OC with diverse mechanical properties. We consider the cells of OC are mechanically different and the communication can be between cells of same type and cells of different types.
B. Base region (30P) of E18.5 OC from the control (*Emx2 Cre*$^{++-}$*:: Vinculin* $^{fl/fl}$) and mutant for vinculin (*Emx2 Cre*$^{+/-}$*:: Vinculin* $^{fl/fl}$) stained for f-actin (green) and Arl13b (magenta). Arrow represents the disrupted organisation of Inner border cells.
C. Polar coordinates representing the Kinocilium position of IHC from control (orange) and vinculin mutant (blue) at base region(30P) of OC. N=66/66 (control/Mutant)
D. Polar coordinates representing the Kinocilium position of OHC from control (orange) and vinculin mutant (blue) at base region(30P) of OC. N= 68/68 (control/Mutant).
E. Apical surface area of IHC from control (orange) and vinculin mutant (blue) at base region(30P) of OC. N=66/66 (Control/Mutant)
F. Apical surface area of IHC from control (orange) and vinculin mutant (blue) at base region(30P) of OC. N=66/66 (Control/Mutant)
G. KO of base region of OC (30P) from control and Vinculin mutant OC stained for F-actin (grey).
H. Apical surface area of medial and lateral KO cells from base region (30P) of control and Vinculin mutant OC. N=145/165 (Control/Mutant)
I. Rose stack plots representing the axis of cell elongation in medial and lateral KO cells from base region (30P) of control and Vinculin mutant OC. N=145/165 (Control/Mutant)

Scale Bar: 5 µm in B and 10 µm in G
Unpaired T-test.
Image orientation: Top is lateral, Right is Apex.

SUPPLEMENTARY FIGURES LEGENDS

Figure S1. Cellular organisation is maintained during convergent extension mediated elongation of OC.

A. Schematic representing the organization of various sensory and non-sensory domains and their constituent cell types in the mouse organ of Corti.
B. OC from E15.5 and E18.5 stained for Myosin 7a.
C. Length of cochlea from E15.5 to post-natal day 2. N=3 embryos for each stage.
D. Base of OC from E15.5 and E18.5 stained for F-actin. The Asterisk indicates lateral non-sensory domain cells, Hensen's in magenta and Claudius in cyan. The green arrowhead indicates the inner border cells and magenta indicates border cells. Cyan arrowhead indicates the medial non-sensory cells, KÖlliker's Organ.
E. Base of E15.5 and E18.5 OC stained for F-actin (green) and p75NTR (magenta).
F. Base of E15.5 and E18.5 OC stained for F-actin (green) and Myosin 7a (magenta).
G. Base of E15.5 and E18.5 OC stained for F-actin (green) and BLBP (magenta).

Scale Bar: 50µm in B and 5µm in D-G
Image orientation: Top is lateral, Right is Apex.

Figure S2. Cellular organisation is preserved in the middle and apex part of looptail mutant OC with defective convergent extension.

A. Middle of E18.5 OC from heterozygous (*Vangl2* $^{Lp/+}$) and homozygous (*Vangl2* $^{Lp/Lp}$) looptail mutant stained for F-actin (green) and Myosin 7a (magenta and grey). N= 4.
B. Middle of E18.5 OC from heterozygous (*Vangl2* $^{Lp/+}$) and homozygous (*Vangl2* $^{Lp/Lp}$) looptail mutant stained for F-actin (green) and p75NTR (magenta and grey). N= 4.
C. Middle of E18.5 OC from heterozygous (*Vangl2* $^{Lp/+}$) and homozygous (*Vangl2* $^{Lp/Lp}$) looptail mutant stained for F-actin (green) and BLBP (magenta and grey). N= 4.
D. Apex of E18.5 OC from heterozygous (*Vangl2* $^{Lp/+}$) and homozygous (*Vangl2* $^{Lp/Lp}$) looptail mutant stained for F-actin (green) and Myosin 7a (magenta and grey). N= 4.
E. Apex of E18.5 OC from heterozygous (*Vangl2* $^{Lp/+}$) and homozygous (*Vangl2* $^{Lp/Lp}$) looptail mutant stained for F-actin (green) and p75NTR (magenta and grey). N= 4.
F. Apex of E18.5 OC from heterozygous (*Vangl2* $^{Lp/+}$) and homozygous (*Vangl2* $^{Lp/Lp}$) looptail mutant stained for F-actin (green) and BLBP (magenta and grey). N= 4.

Scale Bar: 5µm
Image orientation: Top is lateral, Right is Apex.

Figure S3. Radial patterning cues regulate development of adhesion-code.

A. E18.5 OC stained for F-actin (green) and Zona Occludens 1 (ZO1, magenta and grey).
B. E18.5 OC stained for F-actin (green) and Nectin1(magenta and grey).
C. E14.5 OC stained for F-actin (green) and Cdh1(magenta and grey).
D. E14.5 OC stained for F-actin (green) and Cdh2(magenta and grey).

E. E14.5 OC stained for F-actin (green) and Cdh4(magenta and grey). Image is medially shifted to show the expression in the KO.
F. Schematic representing the differential expression of adhesion molecule defined as adhesion-code at E14.5 and the possibility of radial patterning cues to regulate this adhesion code.
G. E14.5 OC from control (*Six1enh21Cre*$^{+/+}$*::Fgfr1*$^{fl/fl}$) and fgfr1 mutant (*Six1enh21Cre*$^{+/-}$*:: Fgfr1*$^{fl/fl}$) cochlea stained for F-actin (green) and Cdh1 (magenta and grey). N=3 embryos.
H. E14.5 OC from control (*Six1enh21Cre*$^{+/+}$*::Fgfr1*$^{fl/fl}$) and fgfr1 mutant (*Six1enh21Cre*$^{+/-}$*:: Fgfr1*$^{fl/fl}$) cochlea stained for F-actin (green) and Cdh2 (magenta and grey). N=3 embryos.

Scale Bar: 10µm
Image orientation: Top is lateral, Right is Apex.
Six1enh21Cre$^{+/+}$ means cre negative and *Six1enh21Cre*$^{+/-}$ cre positive

Figure S4. Disruption of Fgfr1 signalling leads to disruption of adhesion code and cellular organisation in mouse OC.

A. E18.5 OC from Fgfr1 mutant embryos (*Six1enh21Cre*$^{+/-}$*::Fgfr1*$^{fl/lf}$) stained for F-actin showing hair cells as small clusters along the OC, called island phenotype.
B. Schematic representing the development of adhesion code during development in mouse OC.
C. E18.5 OC from control embryos (*Six1enh21Cre*$^{+/+}$*::Fgfr1*$^{fl/fl}$) stained for Cdh1 (grey and magenta), Cdh2 (grey and green) and F-actin (grey in merged). Asterisk indicates the absence of Cdh2 signals from lateral non-sensory domain. N=4 embryos
D. E18.5 OC from Fgfr1 mutant embryos (*Six1enh21Cre*$^{+/-}$*::Fgfr1*$^{fl/fl}$) stained for Cdh1 (grey and magenta), Cdh2 (grey and green) and F-actin (grey in merged). Asterisk indicates the ectopic Cdh2 signals from lateral non-sensory domain. N=4 embryos
E. E18.5 OC from control and Fgfr1 mutant embryos (*Six1enh21Cre*$^{+/-}$*::Fgfr1*$^{fl/fl}$) stained for F-actin (green) and HC marker Beta Spectrin II (magenta). Asterisk indicates the presence of HCs in the lateral and medial non-sensory domains. N=4 embryos

Scale Bar: 10µm
Image orientation: Top is lateral, Right is Apex.
Six1enh21Cre$^{+/+}$ means cre negative and *Six1enh21Cre*$^{+/-}$ cre positive

Figure S5. Adhesion code is maintained in looptail mutants with defective convergent extension.

A. E18.5 OC from heterozygous (*Vangl2* $^{Lp/+}$) and homozygous (*Vangl2* $^{Lp/Lp}$) looptail mutant stained for F-actin (green) and Cdh1 (magenta and grey). N= 3 cochlea
B. E18.5 OC from heterozygous (*Vangl2* $^{Lp/+}$) and homozygous (*Vangl2* $^{Lp/Lp}$) looptail mutant stained for F-actin (green) and Cdh2 (magenta and grey). N= 3 cochlea
C. E18.5 OC from heterozygous (*Vangl2* $^{Lp/+}$) and homozygous (*Vangl2* $^{Lp/Lp}$) looptail mutant stained for F-actin (green) and Cdh4 (magenta and grey). N= 3 cochlea

D. E18.5 OC from heterozygous (*Vangl2* $^{Lp/+}$) and homozygous (*Vangl2* $^{Lp/Lp}$) looptail mutant stained for F-actin (green) and Nectin1 (magenta and grey). N= 3 cochlea

Scale Bar: 10µm

Image orientation: Top is lateral, Right is Apex.

Figure S6. Medial and Lateral sensory domain acquires cellular organisation during development.

A. Schematic of OC representing the 9 equidistant points along the base-apex axis of the OC.
B. Middle (50P) position of OC from E15.5, E16.5 and E18.5 stained for F-actin (green) and Arl13b (magenta).
C. Apex (80P) position of OC from E15.5, E16.5 and E18.5 stained for F-actin (green) and Arl13b (magenta).
D. OC from E16.5 stained for F-actin (green) and cell cycle exit marker, Cdkn1b (magenta).
E. Apical surface area of Outer HC (OHC, red), Dieter's cell (DC, light grey), Inner HC (IHC, yellow), Inner phalangeal cells (IPhC, dark grey) at the base(30P) position of OC from E15.5, E16.5 and E18.5. N= 78/82/84 for OHC, 73/83/84 for DC, 62/65/68 for IHC, 58/62/67 for IPhC (E15.5/E16.5/E18.5).
F. Circularity of Outer HC (OHC, red), and Inner HC (IHC, yellow) at the base(30P) position of OC from E15.5, E16.5 and E18.5. N= 159/189/215 for IHC and 246/249/260 for OHC (E15.5/E16.5/E18.5).

Scale Bar: 5µm in B, C and 10µm in D.

Image orientation: Top is lateral, Right is Apex.

Figure S7. Concurrent development of spatial and orientational order in medial and lateral sensory domain.

A. Schematic representing the calculation of relative pairwise distance in base-apex axis (X) and medio-lateral axis (Y).
B. Relative pairwise distance of IHC (yellow) and OHC (red) along the base-apex axis (X) at E15.5,16.5 and 18.5. N=4 cochlea for each stage
C. Relative pairwise distance of IHC (yellow) and OHC (red) along the medio-lateral axis (Y) at E15.5,16.5 and 18.5. N=4 cochlea for each stage
D. Schematic representing the calculation of hexatic order parameter in the lateral sensory domain.
E. Hexatic order parameter of OHCs at base of OC at E15.5, 16.5 and 18.5. N=3 cochlea for each stage.
F. Hexatic order parameter of OHCs at middle of OC at E15.5, 16.5 and 18.5. N=3 cochlea for each stage.
G. Hexatic order parameter of OHCs at apex of OC at E15.5, 16.5 and 18.5. N=3 cochlea for each stage.

H. Polar plots represent the position of Kinocilia of IHC (orange) and OHC (blue) at base, middle and apex of OC at E15.5,16.5 and 18.5. The position of kinocilia is normalised to the surface area of HCs. Arrow represents the mean angle and the length of arrow indicates the 1-circular variance, where larger the length tighter the distribution.
I. Circular standard deviation (CSD) of OHC polarity over hexatic order for E15.5, E16.5 and 18.5. N=8 for each stage
J. Circular standard deviation (CSD) of IHC polarity over relative pairwise distance (X) for E15.5, E16.5 and E18.5. N=4 for each stage
K. Circular standard deviation (CSD) of IHC polarity over relative pairwise distance (Y) for E15.5, E16.5 and E18.5. N=4 for each stage

Image orientation: Top is lateral, Right is Apex.

R^2 is the coefficient from regression analysis, where values higher than 0.5 suggest a correlation. See Methods for detail.

Figure S8. Cellular rearrangement driven elongation of medial and lateral sensory domain.

A. Schematic of OC representing the 9 equidistant points along the base-apex axis of the OC.
B. Width of the lateral sensory domain along the 9 positions along the base-apex axis at E15.5 and E18.5. N=4 cochlea each stage
C. Width of the medial sensory domain along the 9 positions along the base-apex axis at E15.5 and E18.5. N=4 cochlea each stage
D. OC from E15.5 and E18.5 base position (30P) stained for F-actin (grey), overlayed with red circles representing vertex with 4 or more cells.
E. Percentage of vertex with 4 or more cells in the sensory domain at E15.5 and E18.5. N=3 embryos each with 205/615 for E15.5 and 122/625 for E18.5 (4 or more cell vertices /Total vertices).

Image orientation: Top is lateral, Right is Apex.

Figure S9: Medial and lateral KÖlliker's organ develops spatial ordering during development.

A. KO from middle region (50P) of E15.5 and E18.5 OC stained for F-actin (grey).
B. Rose stack plot representing the axis of elongation for medial and lateral KO cells at middle region (50P) of E15.5 and E18.5 OC. N=185/195 for E15.5 and 215/205 for E18.5 (mKO/lKO).
C. KO from apex region (80P) of E15.5 and E18.5 OC stained for F-actin (grey).
D. Rose stack plot representing the axis of elongation for medial and lateral KO cells at middle region (50P) of E15.5 and E18.5 OC. . N=198/189 for E15.5 and 234/212 for E18.5 (mKO/lKO).
E. Apical surface area of medial and lateral KO cells at middle region (50P) of E15.5 and E18.5 OC. N=185/195 for E15.5 and 215/205 for E18.5 (mKO/lKO).

F. Apical surface area of medial and lateral KO cells at middle region (50P) of E15.5 and E18.5 OC. N=185/195 for E15.5 and 215/205 for E18.5 (mKO/lKO).
G. Representation of apical surface area of KO at E15.5 and E18.5.
H. Percentage of vertex with 4 or more cells in the medial and lateral KO domain at E15.5 and E18.5. N= 3 cochlea each, 498/1070 mKO at E15.5 and 259/630 at E18.5; 318/1532 lKO at E15.5 and 111/835 at E18.5 (4 or more cell vertices /Total vertices)

Scale Bar: 10µm
Unpaired T-test
Image orientation: Top is lateral, Right is Apex.

Figure S10. Cells of lateral non-sensory domain increases in apical surface area during development.

A. Base region (30P) of E16.5 and E18.5 OC stained for F-actin.
B. Apical surface area of Hensen's and Claudius cells at base region of OC at E16.5 and E18.5. N=64/60 for Hensen and 57/59 for Claudius (E16.5/E18.5).
C. Middle region (50P) of E16.5 and E18.5 OC stained for F-actin.
D. Apical surface area of Hensen's and Claudius cells at middle region of OC at E16.5 and E18.5. N=40/51 for Hensen and 39/48 for Claudius (E16.5/E18.5).
E. Apex region (30P) of E16.5 and E18.5 OC stained for F-actin.
F. Apical surface area of Hensen's and Claudius cells at Apex region of OC at E16.5 and E18.5. N=46/58 for Hensen and 48/46 for Claudius (E16.5/E18.5).
G. Schematic representing the position of Hensen's and Claudius cells.
H. Shape index (Q=perimeter/sqrt of area) of Hensen's and Claudius cells at E16.5 and E18.5. N=150/169 for Hensen and 144/153 for Claudius (E16.5/E18.5).

Scale Bar: 10µm
Unpaired T-test
Image orientation: Top is lateral, Right is Apex.

Figure S11. Looptail mutant disrupts spatial and orientational order of sensory compartment.

A. Middle turn of E18.5 OC from heterozygous (*Vangl2* $^{Lp/+}$) and homozygous (*Vangl2* $^{Lp/Lp}$) looptail mutant stained for f-actin (green) and Arl13b (magenta).
B. Apical turn of E18.5 OC from heterozygous (*Vangl2* $^{Lp/+}$) and homozygous (*Vangl2* $^{Lp/Lp}$) looptail mutant stained for f-actin (green) and Arl13b (magenta).
C. Polar coordinates representing the position of kinocilia for IHC from middle turn of E18.5 heterozygous (*Vangl2* $^{Lp/+}$,orange) and homozygous (*Vangl2* $^{Lp/Lp}$,blue) looptail mutant OC. N=66/66 (Het/Homo)
D. Polar coordinates representing the position of kinocilia for OHC from middle turn of E18.5 heterozygous (*Vangl2* $^{Lp/+}$,orange) and homozygous (*Vangl2* $^{Lp/Lp}$,blue) looptail mutant OC. N=110/110 (Het/Homo)
E. Polar coordinates representing the position of kinocilia for IHC from apical turn of E18.5 heterozygous (*Vangl2* $^{Lp/+}$,orange) and homozygous (*Vangl2* $^{Lp/Lp}$,blue) looptail mutant OC. N=66/66 (Het/Homo)

F. Polar coordinates representing the position of kinocilia for OHC from apical turn of E18.5 heterozygous (*Vangl2* $^{Lp/+}$,orange) and homozygous (*Vangl2* $^{Lp/Lp}$,blue) looptail mutant OC. N=110/110 (Het/Homo)
G. Apical surface area of IHC at base, middle and apical turn of E18.5 heterozygous (*Vangl2* $^{Lp/+}$,orange) and homozygous (*Vangl2* $^{Lp/Lp}$,blue) looptail mutant OC. N= 75/85 for base, 61/56 for middle and 74/78 for apex (Het/Homo).
H. Apical surface area of OHC at base, middle and apical turn of E18.5 heterozygous (*Vangl2* $^{Lp/+}$,orange) and homozygous (*Vangl2* $^{Lp/Lp}$,blue) looptail mutant OC. N= 105/115 for base, 116/126 for middle and 124/118 for apex (Het/Homo).
I. Relative pairwise distance along base-apex axis (X) for IHC of E18.5 heterozygous (*Vangl2* $^{Lp/+}$,orange) and homozygous (*Vangl2* $^{Lp/Lp}$,blue) looptail mutant OC. N=4 cochlea
J. Relative pairwise distance along base-apex axis (Y) for IHC of E18.5 heterozygous (*Vangl2* $^{Lp/+}$,orange) and homozygous (*Vangl2* $^{Lp/Lp}$,blue) looptail mutant OC. N=4 cochlea
K. Relative pairwise distance along base-apex axis (X) for OHC of E18.5 heterozygous (*Vangl2* $^{Lp/+}$,orange) and homozygous (*Vangl2* $^{Lp/Lp}$,blue) looptail mutant OC. N=4 cochlea
L. Relative pairwise distance along base-apex axis (Y) for OHC of E18.5 heterozygous (*Vangl2* $^{Lp/+}$,orange) and homozygous (*Vangl2* $^{Lp/Lp}$,blue) looptail mutant OC. N=4 cochlea
M. Width of medial sensory domain across OC of E18.5 heterozygous (*Vangl2* $^{Lp/+}$,orange) and homozygous (*Vangl2* $^{Lp/Lp}$,blue) looptail mutant OC. N=4 cochlea
N. Width of lateral sensory domain across OC of E18.5 heterozygous (*Vangl2* $^{Lp/+}$,orange) and homozygous (*Vangl2* $^{Lp/Lp}$,blue) looptail mutant OC. N=4 cochlea

Scale Bar: 5µm
Unpaired T-test, * =P<0.05
Image orientation: Top is lateral, Right is Apex.

Figure S12. Looptail mutant disrupts cellular organisation in KÖlliker's organ.

A. KO from middle region (50P) of E18.5 OC from heterozygous (*Vangl2* $^{Lp/+}$) and homozygous (*Vangl2* $^{Lp/Lp}$*)* looptail mutant stained for F-actin (grey).
B. Rose stack plot representing the axis of elongation for mKO and lKO cells from middle region (50P) of heterozygous (*Vangl2* $^{Lp/+}$) and homozygous (*Vangl2* $^{Lp/Lp}$*)* looptail mutant OC. N=168/144 (mKO/lKO, Het) and 139/148 (mKO/lKO, Homo).
C. KO from apex region (80P) of E18.5 OC from heterozygous (*Vangl2* $^{Lp/+}$) and homozygous (*Vangl2* $^{Lp/Lp}$*)* looptail mutant stained for F-actin (grey).
D. Rose stack plot representing the axis of elongation for mKO and lKO cells from apex region (80P) of heterozygous (*Vangl2* $^{Lp/+}$) and homozygous (*Vangl2* $^{Lp/Lp}$*)* looptail mutant OC. N=188/194 (mKO/lKO, Het) and 192/187 (mKO/lKO, Homo).
E. Apical surface area of mKO and lKO cells from middle region (50P) of heterozygous (*Vangl2* $^{Lp/+}$) and homozygous (*Vangl2* $^{Lp/Lp}$*)* looptail mutant OC. N=168/144 (mKO/lKO, Het) and 139/148 (mKO/lKO, Homo).

F. Apical surface area of mKO and lKO cells from middle region (50P) of heterozygous (*Vangl2* $^{Lp/+}$) and homozygous (*Vangl2* $^{Lp/Lp}$) looptail mutant OC. N=188/194 (mKO/lKO, Het) and 192/187 (mKO/lKO, Homo).
G. Schematic representation of apical surface area of KO cells in heterozygous and homozygous looptail mutant OC showing reduction in difference between medial and lateral KO cells.

Scale Bar: 10µm
Image orientation: Top is Lateral, Right is Apex.
Unpaired T-test

Figure S13. Conditional knockout of Vangl2 from inner ear disrupts cellular organisation in compartments with limited effect on domain sculpting.

A. Schematic representing the mating scheme to generate control and experimental animals for conditional deletion of *Vangl2* allele.
B. Length of cochlea from control (S*ox10cre*$^{+/+}$*:: Vangl2*$^{lp/fl}$) in orange and mutant (*Sox10cre*$^{+/-}$*:: Vangl2*$^{lp/fl}$) in blue. N=3 cochlea each from control and mutant.
C. Width of KO compartment across control (in orange) and mutant (blue) OC at E18.5. N=3 cochlea each from control and mutant.
D. Width of sensory compartment across control (in orange) and mutant (blue) OC at E18.5.
E. Base region (30P) of control and mutant OC stained for F-actin (green) and Arl13b (magenta).
F. Polar coordinates representing the position of kinocilia of IHC at base region of control (orange) and mutant OC (blue). N=78/71 (control/mutant)
G. Polar coordinates representing the position of kinocilia of OHC at base region of control (orange) and mutant OC (blue). N=123/121 (control/mutant)
H. Apical surface area of IHC at base region of control (orange) and mutant OC (blue). N=76/57 (control/mutant)
I. Circularity of IHC at base region of control (orange) and mutant OC (blue). N=76/57 (control/mutant)
J. Apical surface area of OHC at base region of control (orange) and mutant OC (blue).N=202/130 (control/mutant)
K. Circularity of IHC at base region of control (orange) and mutant OC (blue). N=202/130 (control/mutant)
L. KÖlliker's organ from base region (30P) of control and mutant OC stained for F-actin (grey).
M. Rose stack plot representing the axis of elongation for medial and lateral KO cells at base region (30P) of control and mutant OC. N=134/128 for control and 180/176 for mutant (mKO/lKO)
N. Apical surface area of mKO and lKO cells at the base region (30P) of control and mutant OC. N=134/128 for control and 180/176 for mutant (mKO/lKO).

Scale Bar: 5µm for E and 10µm for L
Image orientation: Top is lateral, Right is Apex.
Unpaired T-test. ns= non-significant.

Figure S14. Vangl2 regulates NMII activity through RLC phosphorylation.

A. E18.5 OC stained for F-actin (green) and mono-phosphorylated form of RLC (pRLC, magenta, grey).
B. KO from E18.5 OC stained for ZO1(green) and di-phosphorylated form of RLC (ppRLC, magenta, grey).
C. Sensory domain from E18.5 OC stained for ZO1(green) and di-phosphorylated form of RLC (ppRLC, magenta, grey). Scale Bar: 5µm
D. Sensory domain from E18.5 OC stained for F-actin (green) and Vangl2 (magenta).
E. E18.5 OC from heterozygous looptail mutant stained for F-actin (green) and pRLC (magenta, grey).
F. E18.5 OC from homozygous looptail mutant stained for F-actin (green) and pRLC (magenta, grey).
G. E18.5 OC from heterozygous looptail mutant stained for ZO1(green) and ppRLC (magenta, grey).
H. E18.5 OC from homozygous looptail mutant stained for ZO1(green) and ppRLC (magenta, grey).

Scale Bar: 10µm except C,D (5µm).
Image orientation: Top is lateral, Right is Apex.

Figure S15. ROCK inhibition disrupts the spatial and orientational order of OC.

A. E16.5 cochlea cultured ex-vivo for 8 hours in a 3D-collagen droplet culture with DMEM and stained for F-actin (green) and pRLC (magenta, grey). N=6 cochlea
B. E16.5 cochlea cultured ex-vivo for 8 hours in a 3D-collagen droplet culture with DMEM supplemented with 10µM Y-27632, stained for F-actin (green) and pRLC (magenta, grey). N=6 cochlea
C. E16.5 cochlea cultured ex-vivo for 8 hours in a 3D-collagen droplet culture with DMEM and stained for ZO1 (green) and ppRLC (magenta, grey). N=6 cochlea
D. E16.5 cochlea cultured ex-vivo for 8 hours in a 3D-collagen droplet culture with DMEM supplemented with 10µM Y-27632, stained for ZO1 (green) and ppRLC (magenta, grey). N=6 cochlea
E. E16.5 cochlea cultured ex-vivo for 8 hours in a 3D-collagen droplet culture with DMEM and supplemented with 10µM Y-27632, stained for F-actin (green) and Arl13b (magenta). N=6 cochlea
F. Polar coordinates representing position of kinocilia of IHC from OC cultured in presence (blue) or absence (orange) of ROCK-inhibitor Y-27632. N= 68/67 (DMEM/Y-27632)
G. Polar coordinates representing position of kinocilia of OHC from OC cultured in presence (blue) or absence (orange) of ROCK-inhibitor Y-27632. N= 82/84 (DMEM/Y-27632)

H. Circularity of IHC and OHC from OC cultured in presence (blue) or absence (orange) of ROCK-inhibitor Y-27632. N=53/57 for IHC and 87/89 for OHC (DMEM/Y-27632)
I. Apical surface area of IHC and OHC from OC cultured in presence (blue) or absence (orange) of ROCK-inhibitor Y-27632. N=53/57 for IHC and 87/89 for OHC (DMEM/Y-27632).
J. Apical surface area of mKO and lKO cells from OC cultured in presence or absence of ROCK-inhibitor Y-27632.
K. Rose stack plot representing the axis of cell elongation for mKO and lKO cells in OC cultured in DMEM. N= 223/243 mKO/lKO.
L. Rose stack plot representing the axis of cell elongation for mKO and lKO cells in OC cultured in DMEM. N= 213/254 mKO/lKO.

Image orientation: Top is lateral, Right is Apex.
Scale Bar: 10µm
Unpaired T-test

Supplementary Figure S16. MLCK inhibition disrupts the spatial and orientational order of OC.

A. E16.5 cochlea cultured ex-vivo for 8 hours in a 3D-collagen droplet culture with DMEM supplemented with DMSO and stained for F-actin (green) and pRLC (magenta, grey). N=6 cochlea
B. E16.5 cochlea cultured ex-vivo for 8 hours in a 3D-collagen droplet culture with DMEM supplemented with 25µM ML7, stained for F-actin (green) and pRLC (magenta, grey). N=6 cochlea
C. E16.5 cochlea cultured ex-vivo for 8 hours in a 3D-collagen droplet culture with DMEM supplemented with DMSO and stained for ZO1 (green) and ppRLC (magenta, grey). N=6 cochlea
D. E16.5 cochlea cultured ex-vivo for 8 hours in a 3D-collagen droplet culture with DMEM supplemented with 25µM ML7, stained for ZO1 (green) and ppRLC (magenta, grey). N=6 cochlea
E. E16.5 cochlea cultured ex-vivo for 8 hours in a 3D-collagen droplet culture with DMEM supplemented with DMSO or 25µM ML7, stained for F-actin (green) and Arl13b (magenta). N=6 cochlea
F. Polar coordinates representing position of kinocilia of IHC from OC cultured in presence (blue) or absence (orange) of MLCK-inhibitor ML7. N= 66/68 (DMSO/ML7)
G. Polar coordinates representing position of kinocilia of OHC from OC cultured in presence (blue) or absence (orange) of MLCK-inhibitor ML7. N= 68/61 (DMSO/ML7)
H. Circularity of IHC and OHC from OC cultured in presence (blue) or absence (orange) of MLCK-inhibitor ML7. N=58/61 for IHC and 69/66 for OHC (DMSO/ML7)

I. Apical surface area of IHC and OHC from OC cultured in presence (blue) or absence (orange) of MLCK-inhibitor ML7. N=58/61 for IHC and 69/66 for OHC (DMSO/ML7).
J. Apical surface area of mKO and lKO cells from OC cultured in presence or absence of MLCK-inhibitor ML7. N= 193/207 for DMSO and 203/214 for ML7 (DMSO/ML7).
K. Rose stack plot representing the axis of cell elongation for mKO and lKO cells in OC cultured in DMSO. N= 193/207 mKO/lKO.
L. Rose stack plot representing the axis of cell elongation for mKO and lKO cells in OC cultured in ML7. N= 203/214 mKO/lKO.

Image orientation: Top is lateral, Right is Apex.
Scale Bar: 10µm
Unpaired T-test, ns=non-signficant, P>0.05

METHODS

Mice

Animal housing

All mice were housed at Animal Care and Resource Centre (ACRC) at NCBS, in accordance with Institutional Animal Ethics Committee guidelines.

Mouse strains

The supplementary table below provides information about the mouse strains used.

Table S1: Mouse strains used for experiments in this paper:

Mouse strain	Identifier	Source
Vangl2 (looptail)	JAX:000220	Jackson Laboratory
Vangl2 Flox	JAX: 025174	Jackson Laboratory
TdtomatoAi14	JAX: 007914	Jackson Laboratory
Fgfr1 Flox	NA	Ulla Pirvola 2002
Emx2 Cre	NA	Jun Kimura 2005
Sox10 Cre	JAX:025807	Jackson Laboratory
Six1enh21 Cre	NA	Shigeru Sato 2012
Ngn1-457 Cre	JAX:012859	Jackson Laboratory
Lgr5-IRES-CREERT2	JAX:008875	Jackson Laboratory
Vinculin Flox	NA	Alice E. Zemljic-Harpf 2007

Genotyping

For maintaining stock animals of strains, an ear biopsy was collected from P21-P30 animals. Each biopsy was lysed in 150µl lysis solution (250ul of 1M NaOH, 2ul of 1M EDTA in 9.748 ml of autoclaved water) for 1 hour at 95°C in a 1.5ml microcentrifuge tube and then

stored after adding 150µl neutralising solution (0.4ml of 1M Tris-Cl in 9.6ml of autoclaved water). 1µl of this solution was used as template for polymerase chain reaction (PCR) based genotyping. A 10µl of PCR mixture contained 5µl of Kappa-2X genotyping master mix (Cat# KK1024, Roche), 0.5µl each of reverse and forward primer and 3µl of nuclease free water. The PCR was performed as per manufacturer protocol and the oligonucleotide used as primers is listed in Table S2.

Table S2: Oligonucleotide sequences used for PCR-based genotyping mouse strains

Name	Oligonucleotide Sequence 5'- 3'	Annealing Temperature
Vangl2 Flox FWD	CAGAATCCTCCTGTCCCTGA	59°C
Vangl2 Flox REV	CTCAGCTAAACCACCTCTGC	
Cre FWD	TGCCAGGATCAGGGTTAAAGAT	60°C
Cre REV	AGCTTGCATGATCTCCGGTATT	
FGFR1 FWD	AATAGGTCCCTCGACGGTATC	60°C
FGFR1 REV	CTGGGTCAGTGTGGACAGTGT	
Vinculin FWD	CCTGCGCGGGATTACCTCATTGA	58°C
Vinculin REV	TGCTCACCTGGCCCAAGATTCTT	
TdTomato FWD	GGCATTAAAGCAGCGTATCC	60°C
TdTomato REV	CTGTTCCTGTACGGCATGG	

Looptail mutants were identified with kink to looped tail in heterozygous conditions and with an open neural tube in the homozygous conditions.

Tamoxifen Injection

The age-appropriate female of the *vangl2 fl/fl* genotype was bred with *vangl2 looptail/+; Lgr5* genotype males. Tamoxifen was dissolved in 90% corn oil and 10% ethanol to prepare a

stock concentration of 10mg/ml. Pregnant females were weighed at the E15.5 stage using an electronic balance and were injected intraperitoneally with an appropriate volume of tamoxifen solution at 4.5mg/40g of body mass. As a control, corn oil and ethanol solution without tamoxifen is injected.

Immunostaining

The inner ears from staged mouse embryos were dissected using a pair of forceps in ice-cold Phosphate Buffer Saline (PBS) and then fixed in 4% Paraformaldehyde (PFA) for 30 minutes to overnight according to the primary antibody, See Table S3. The inner ear is further dissected to expose sensory epithelia. The sensory epithelia are then permeabilized using 0.3% Tween-20 in PBS for 30 minutes at room temperature and blocked using blocking solution (5% heat-inactivated goat serum, 1% bovine serum albumin, 0.3% Tween-20 and PBS) for 1 hour at room temperature. Sensory epithelia are then incubated with primary antibodies diluted in a blocking solution (5% heat inactivated goat serum, 1% Bovine Serum Albumin, 0.3% Tween-20 in PBS) for overnight at 4°C. Sensory epithelia are then washed for 4 hours with a change of washing solution (0.3% Tween-20 in PBS) after every 30 minutes. The sensory epithelia are then incubated with secondary antibodies conjugated with Alexa fluor and phalloidin conjugated with Alexa fluor for 1 hour at room temperature and then washed using a washing solution for 3 hours with a change of washing solution after every 30 minutes. The sensory epithelia are then mounted on the glass slide and 0.17mm cover glass using aqueous mounting media

Table S3: Primary and secondary antibodies used with the fixation condition

Antibody	Source	Fixation
Myosin 7a	DSHB 138-1	4% PFA 1 hour RT or 4% PFA overnight

Arl13b	Proteintech 17711-1-AP	4% PFA 1 hour RT or 4% PFA overnight
Beta Spectrin II	BD Biosciences 612562	4% PFA 1 hour RT or 4% PFA overnight
E Cadherin	BD Biosciences 610405	4% PFA 30minutes RT or Glyoxyl fixation 30minutes RT
N Cadherin	BD Biosciences 610920	4% PFA 30minutes RT or Glyoxyl fixation 30minutes RT
E Cadherin	Cell signalling Technology 3295	4% PFA 30minutes RT or Glyoxyl fixation 30minutes RT
P75NTR	Merck AB1554	4% PFA 1 hour RT
BLBP	Abcam ab32423	4% PFA 1 hour RT
Vangl2	Sigma HPA027043	4% PFA 30minutes RT
p-RLC	Cell signalling Technology 3675	4% PFA 30minutes RT
pp-RLC	Cell signalling Technology 3674	4% PFA 30minutes RT and 2%TCA 30minutes on ice
Cdkn1b	sc-1641	4% PFA 1 hour RT
ZO1	Sigma MABT339	4% PFA overnight or 4% PFA 30minutes RT and 2%TCA 30minutes on ice
Nectin 1	MBL 48-12	4% PFA 30minutes RT
Nectin 2	MBL 502-57	4% PFA 30minutes RT
R Cadherin	DSHB MRCD5	4% PFA 30minutes RT or Glyoxyl fixation 30minutes RT
E Cadherin Block	DSHB 7D6	NA
N cadherin Block	DSHB 6B3	NA
Phalloidin 488	Invitrogen A12379	4% PFA 1 hour RT to 4% PFA overnight
Phalloidin 568	Invitrogen A12380	4% PFA 1 hour RT to 4% PFA overnight
Goat anti-Rabbit 488	Invitrogen A11034	In all fixation conditions
Goat anti- Rabbit 594	Invitrogen A11037	In all fixation conditions
Goat anti-Rabbit 647	Invitrogen A21244	In all fixation conditions
Goat anti-mouse 488	Invitrogen A-11001	In all fixation conditions
Goat anti-mouse 594	Invitrogen A-11005	In all fixation conditions
Goat anti-mouse 647	Invitrogen A-21235	In all fixation conditions
Goat anti-rat 594	Invitrogen A-11007	In all fixation conditions

Imaging

The sensory epithelia were imaged using Olympus Fluoview 3000 inverted microscope controlled by Olympus FV31S-SW software at Central Imaging and Flow Cytometry Facility (CIFF) at NCBS. The images were obtained using 60X oil immersion objective of numerical aperture (NA) 1.42. The start and end point of the confocal volume were decided with the presence of stereocilia and junctions; images were obtained with a step size 0.5µm and pixel size as per Nyquist sampling criteria. The laser power was reduced using a neutral density filter (ND filter) to less than 10% and tuned from 0.1% to 10% for each experiment, keeping the voltage values between 400-500V, gain at 1 and offset between 2-3%, images were obtained by line sequential scanning. The light path was chosen such that the primary dichroic mirror and the secondary dichroic mirror were the same for each scanning and emitted light was collected by a high sensitivity spectral detector. For constructing the whole sensory epithelia images, the images were obtained using 10X air objective of NA 0.4 with step size of 1µm, line sequential scanning, HV values ranging between 400-500V.

The Olympus FV31S-SW software converts signals to 16-bit depth. The rotation feature of the software is used to align tissue wherever necessary.

Ex-vivo organ culture

To culture cochlea, we used a three-dimensional collagen droplet culture previously explained (Singh et al 2022). Briefly, we made a collagen matrix solution by mixing 400µl of rat tail collagen I, 50µl of 10X DMEM, 30µl of 7.5% NaHCO3 and 5µl of HEPES using a pipette. Collagen mixture is poured as separate drops in 4-well dishes. The cochlea from the mouse embryo is dissected and a single cochlea is kept in each drop. Once all the drops have received one cochlea each the 4-well plate is transferred to a 37˚C incubator maintaining 5% CO_2 for 5 minutes. The plate is then taken out and the 500µl of culture media (1X DMEM

supplemented with N2 and penicillin) is added using micropipettes and sterilised tips. The plate is then incubated at a 37˚C incubator maintaining 5% CO_2 for the required time. For small molecule perturbation, the solutions of the small molecule are added to the culture media of a well and treated as experiment and the solvent of the compound are added to the culture media and treated as control. For blocking experiments, Bovine Serum Albumin (BSA) was used as a control. The concentration of small molecule inhibitors and blocking antibodies is presented in table S4.

Table S4: Concentration of small molecule inhibitors used for ex-vivo organ culture

Small Molecule Inhibitor	Identifier	Concentration used
Y-27632	Sigma Y0503	10µm
ML7	Sigma 475880	25µm
E cadherin	DSHB 7D6	5µl/ml
N cadherin Block	DSHB 6B3	5µl/ml

Image Analysis

The confocal images obtained were opened in FIJI (NIH Image J) and processed to form single-channel and multichannel merged images. Images were provided with a scale bar using the metadata confocal file. To evaluate the morphological features of the cells in the epithelia we segmented the images using the Tissue-Analyzer plugin and used the segmented images to obtain values of **apical surface area, shape index, circularity, Feret angle, aspect ratio** using the auto-measure tool in Image J. We also obtained other morphological features of the epithelia

A. **Modified Hexatic order:** The modified hexatic order is calculated using the script described in Prakash et al 2023. Briefly, the hexatic order calculates the angular

orientation of centroid of proximate HCs using the formula ψ_6=1/N∑_(n=1)^N e^(i6□_n) $\psi_6 = 1/N\sum_(n = 1)\wedge N\ e\wedge(i6\phi_n)$.

B. **Polarity:** The position of kinocilia is ascertained by the Beta-spectrin2 or Arl13b staining. The X, Y coordinates of the cilia position is determined using Image J and a vector is drawn from the centroid of HCs to the cilia position. This vector length (r) is normalised to the radius of cells and the angle (θ) is with respect to the P-D axis (θ). The cilia position is then plotted along with the calculation of the mean angle (denoted by the angle of the arrow) and circular standard deviation (denoted by the length of the arrow) using the custom-made script, which would be deposited on GitHub after the acceptance of this manuscript.

C. **Relative pairwise distance:** The centroid position of proximate HCs is obtained using the segmented image and NIH image. The distance between the two HCs (D) and the radius of those two HCs are calculated (r1 and r2). The distance between the two HCs is then transformed into X and Y components, and then the Relative pairwise distance was then calculated using the following formula:

$$\delta\,(X) = \frac{X}{r1+r2} \quad \text{and} \quad \delta\,(Y) = \frac{Y}{r1+r2}$$

D. **4-Cell vertex calculations:** The segmented images in Tissue analyser are processed to obtain the data for bonds using SQL command. The data for bond position and vertex coordinates are tabulated in MS Excel. Using a MS Excel macro, the vertex with more than 4 cells and the total number of vertices are computed.

E. **Colour coded apical surface area**: Representative images presented in Figure 3 and 4 showing the apical surface area for KO is obtained using segmented images in Tissue-Analyzer.

F. **Width of the compartments:** For calculation of sensory compartment width a straight line is drawn in FIHI from the medial edge of IHC to the lateral edge of border cells. The

medial sensory compartment is calculated from medial edge of IHC to lateral edge of pillar cells; the lateral sensory compartment is calculated from medial edge of OHC1 to lateral edge of border cells.

Visualisation

Graphs are made using Prism-GraphPad. Rose stack plots representing the axis of elongation for KO cells are plotted using Oriana software from Kovach computing services. The images are assembled into figures using Inkscape.

Statistics

We performed a two-tail unpaired T-test without assuming Gaussian distribution as the Mann-Whitney T-test to calculate the significance level using Prism-GraphPad software.

Supplementary References:

1. Singh, Nishant, Anubhav Prakash, Suraj Ranganath Chakravarthy, Raman Kaushik, and Raj K. Ladher. "In Ovo and Ex Ovo Methods to Study Avian Inner Ear Development." JoVE (Journal of Visualized Experiments) 184 (2022): e64172.
2. Prakash, Anubhav, Julian Weninger, Nishant Singh, Sukanya Raman, Karsten Kruse, Madan Rao, and Raj Ladher. "Junctional Force Patterning drives both Positional and Orientational Order in Auditory Epithelia." (2023).
3. Schindelin, J. et al. Fiji: an open-source platform for biological-image analysis. Nature methods 9, 676-682 (2012).
4. Benoit Aigouy, Benjamin Prud’homme. Segmentation and Quantitative Analysis of Epithelial Tissues. Drosophila, 2540, Springer US, pp.387-399, 2022, Methods in Molecular Biology, ff10.1007/978-1-0716- 2541-5_20ff. ffhal-03844061f

Mechanical coupling of compartments drives polarity and patterning of mouse auditory epithelium

Anubhav Prakash, Sukanya Raman, Raman Kaushik, Anton S Iyer and Raj K Ladher

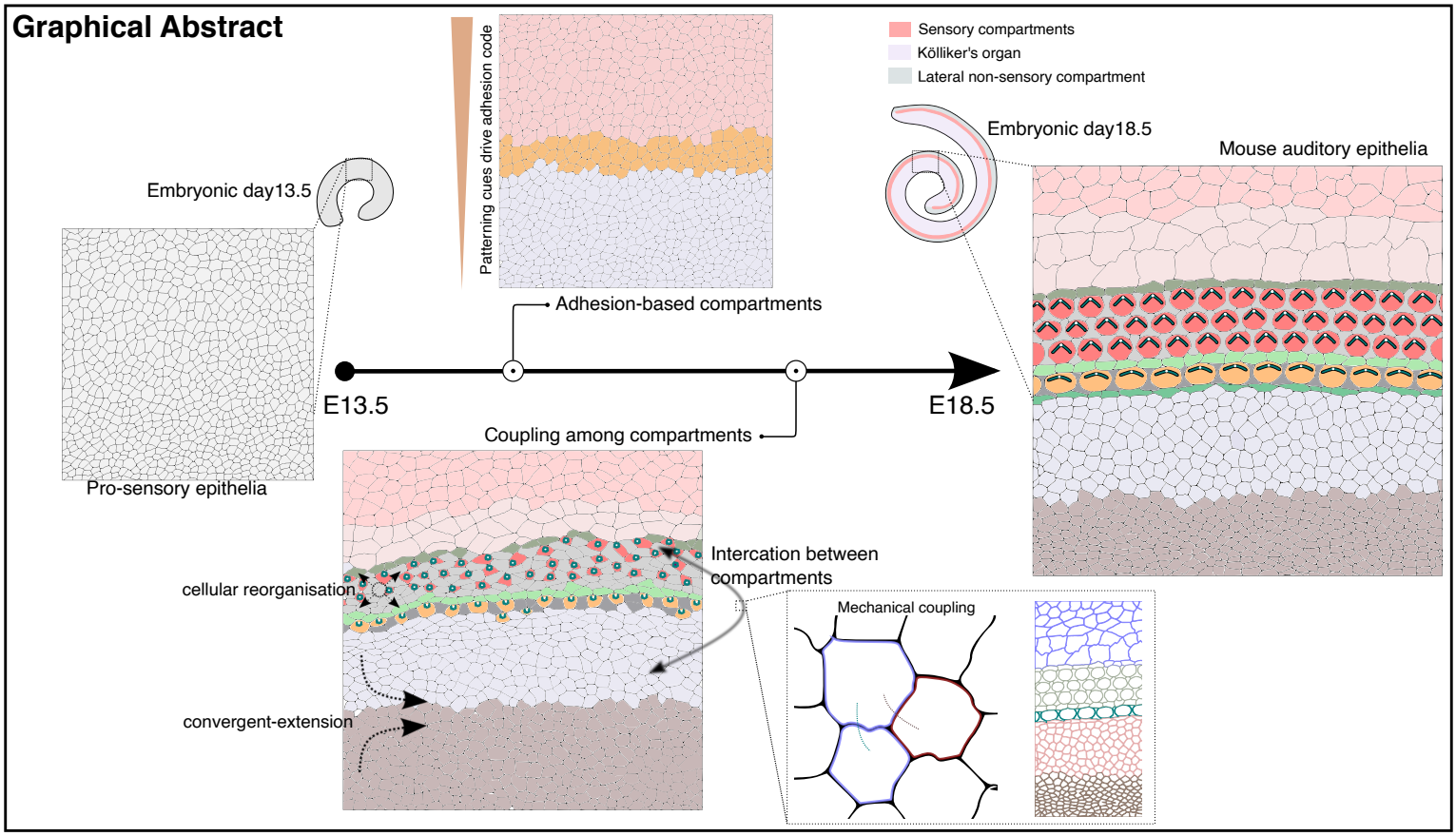

Summary:

The mouse auditory epithelia called Organ of Corti is a compartmentalised epithelium

A differential expression of adhesion molecule driven by FGF signalling provides the adhesion code for compartmentalisation

The cells within these compartments develops discrete phenotypic characteristics driven by cellular intercalations

PCP conditional mutants show compartments interacts with each other

Vinculin mutants show these interaction to have mechanical components

Correspondance:

anubhav.prakash@ashoka.edu.in
rajladher@ncbs.res.in

Figure 1

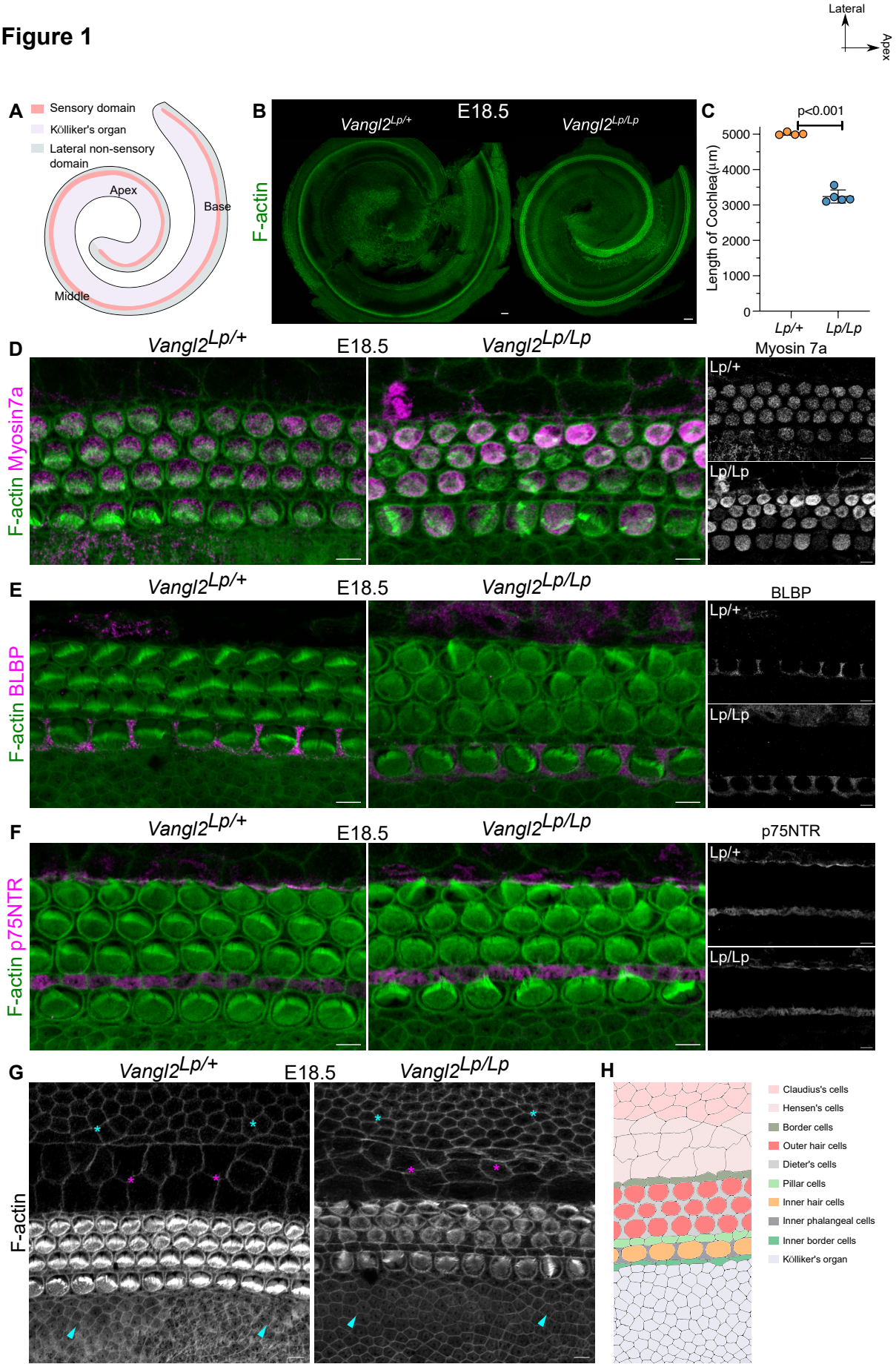

Cellular organisation is preserved in looptail mutants with defective convergent extension.

Figure 2

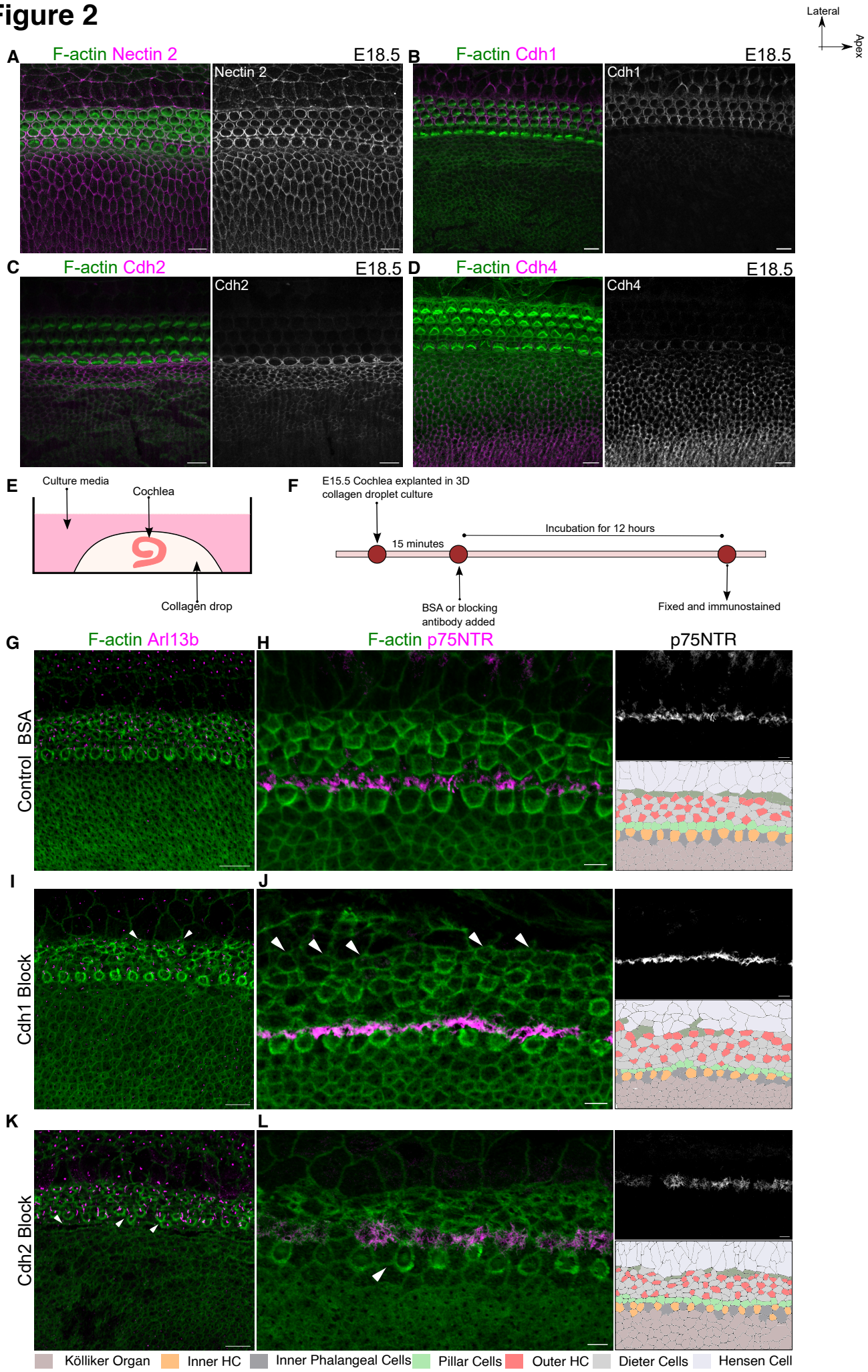

Adhesion-code preserves the cellular organisation during convergent extension mediated extension of OC.

Figure 3

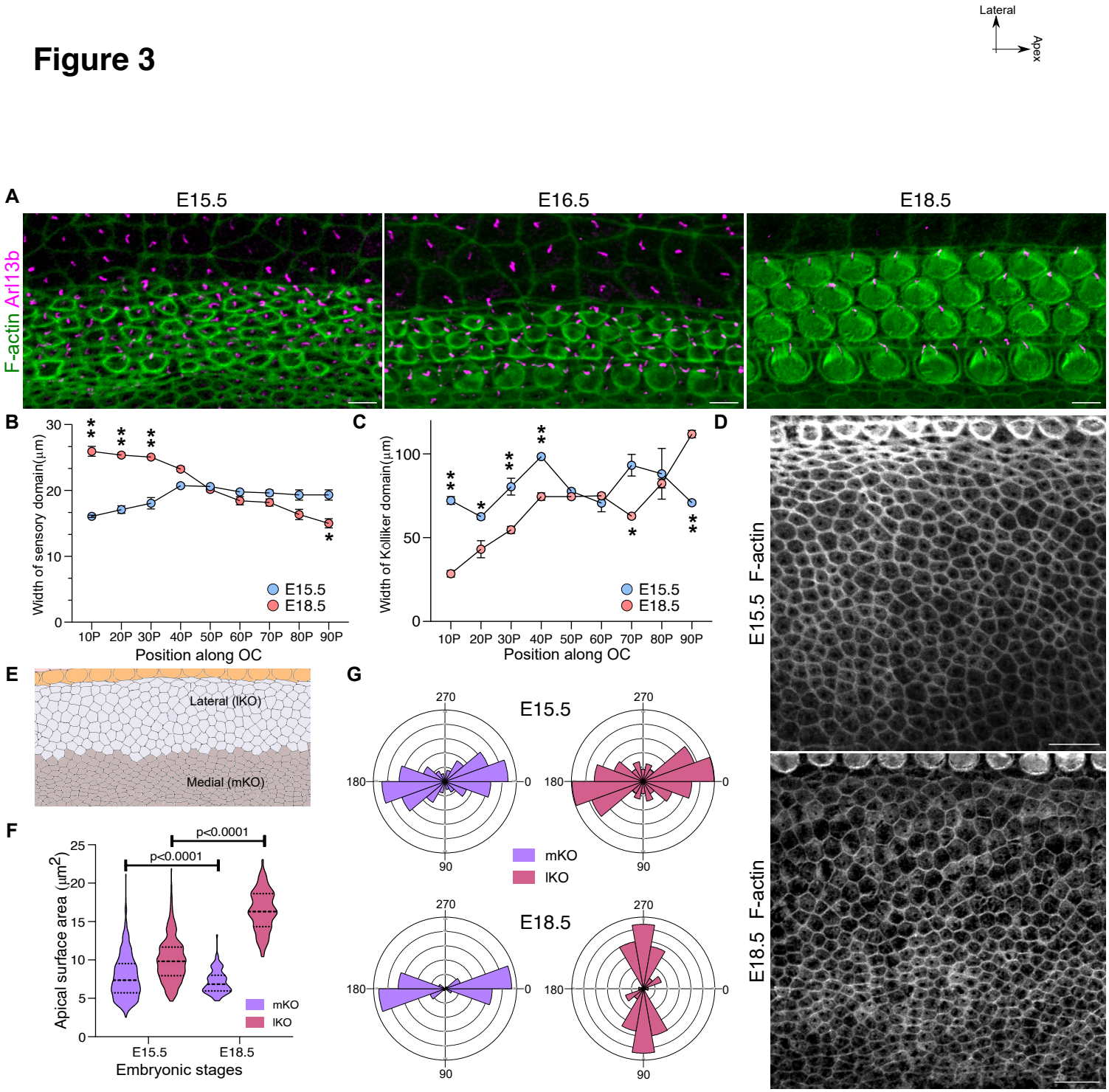

Sensory and non-sensory domain acquires discrete ordering.

Figure 4

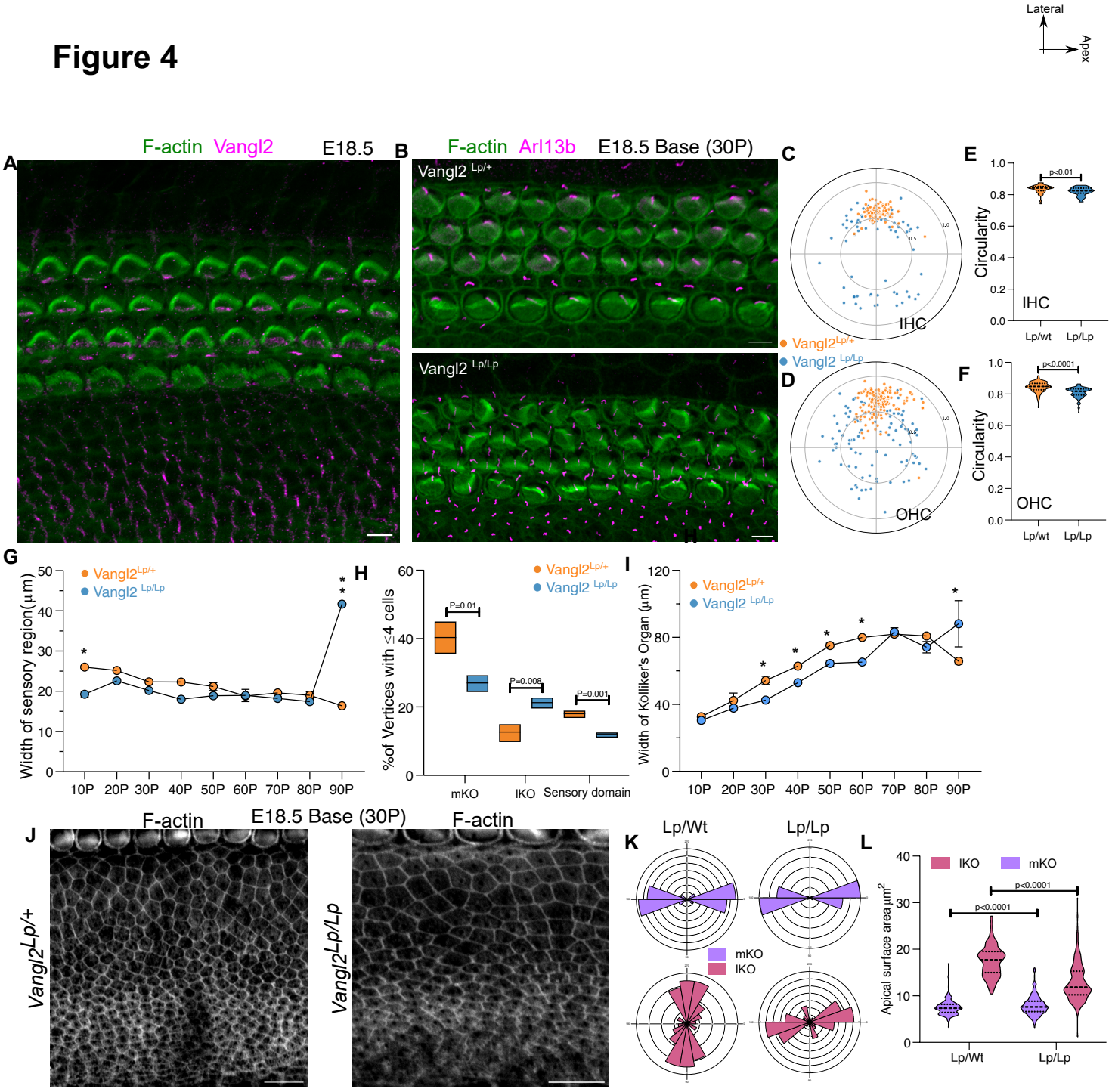

Looptail mutant disrupts organisation in each compartment.

Figure 5

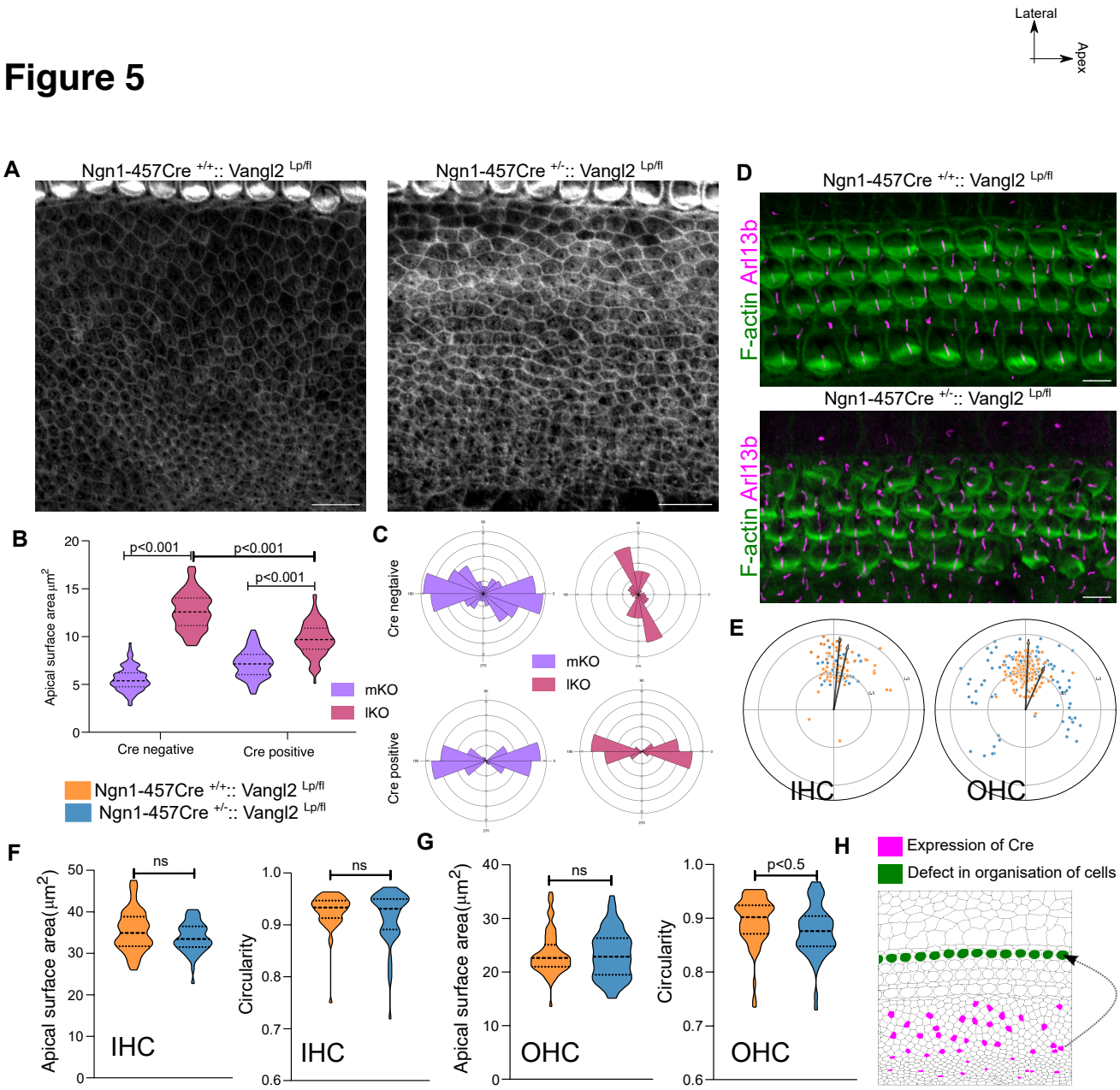

Deletion of Vangl2 from Kolliker's organ disrupts organisation in lateral sensory domain.

Figure 6

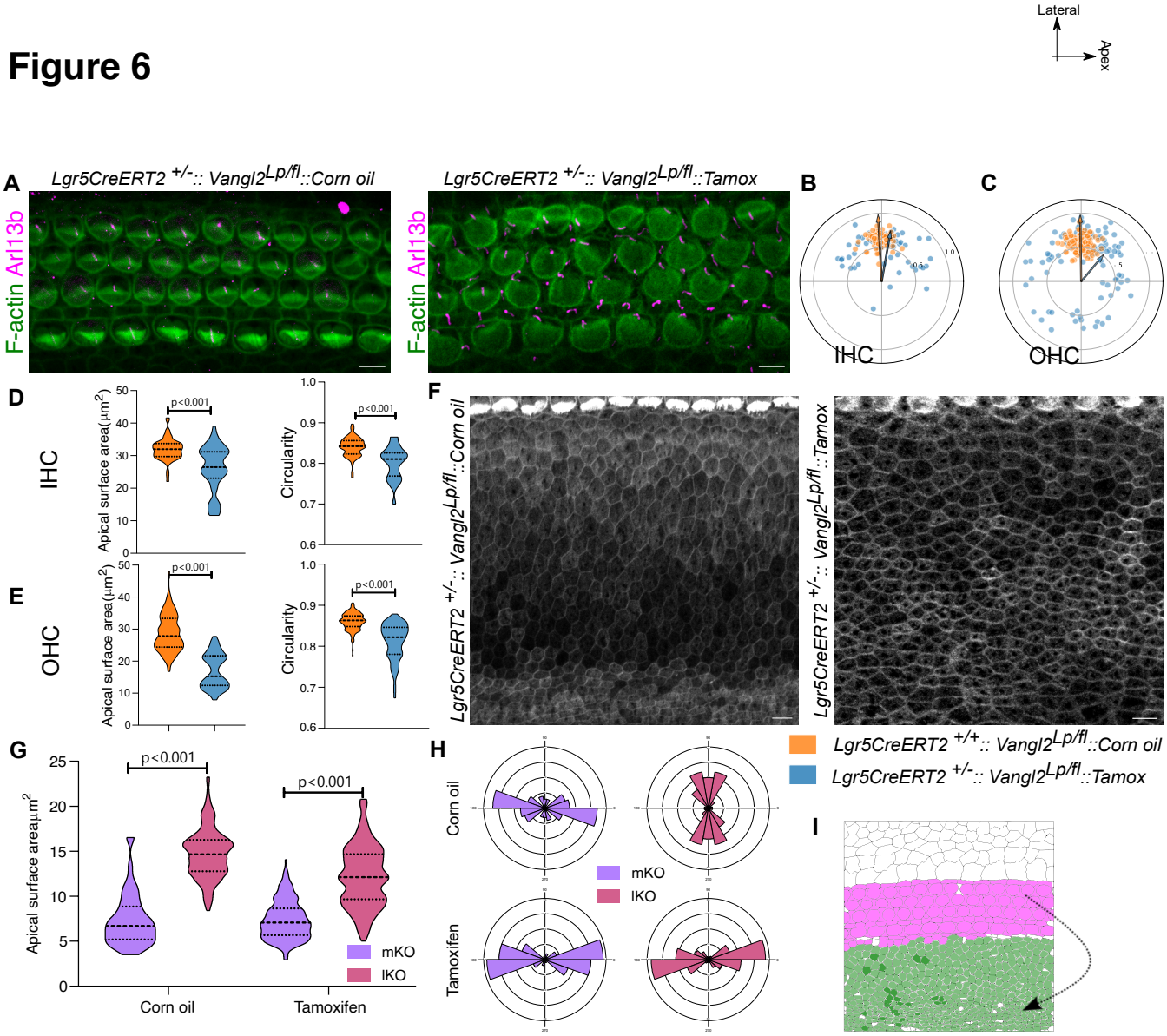

Deletion of Vangl2 from sensory compartments disrupts organisation in KO compartment.

Figure 7

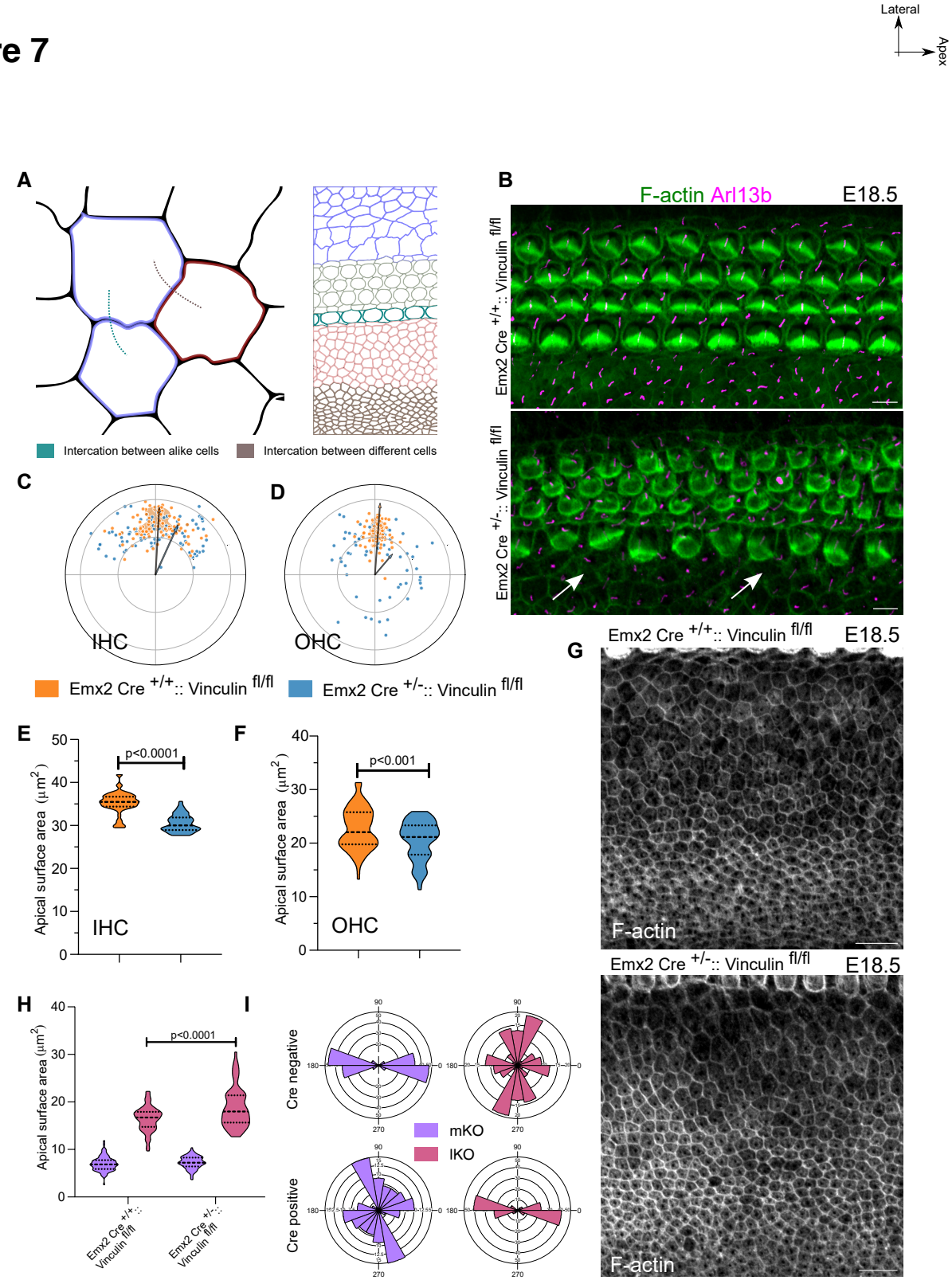

Disruption of Junctional force transmission complex protein, Vinculin, disrupts the organisation of OC.

Figure S1

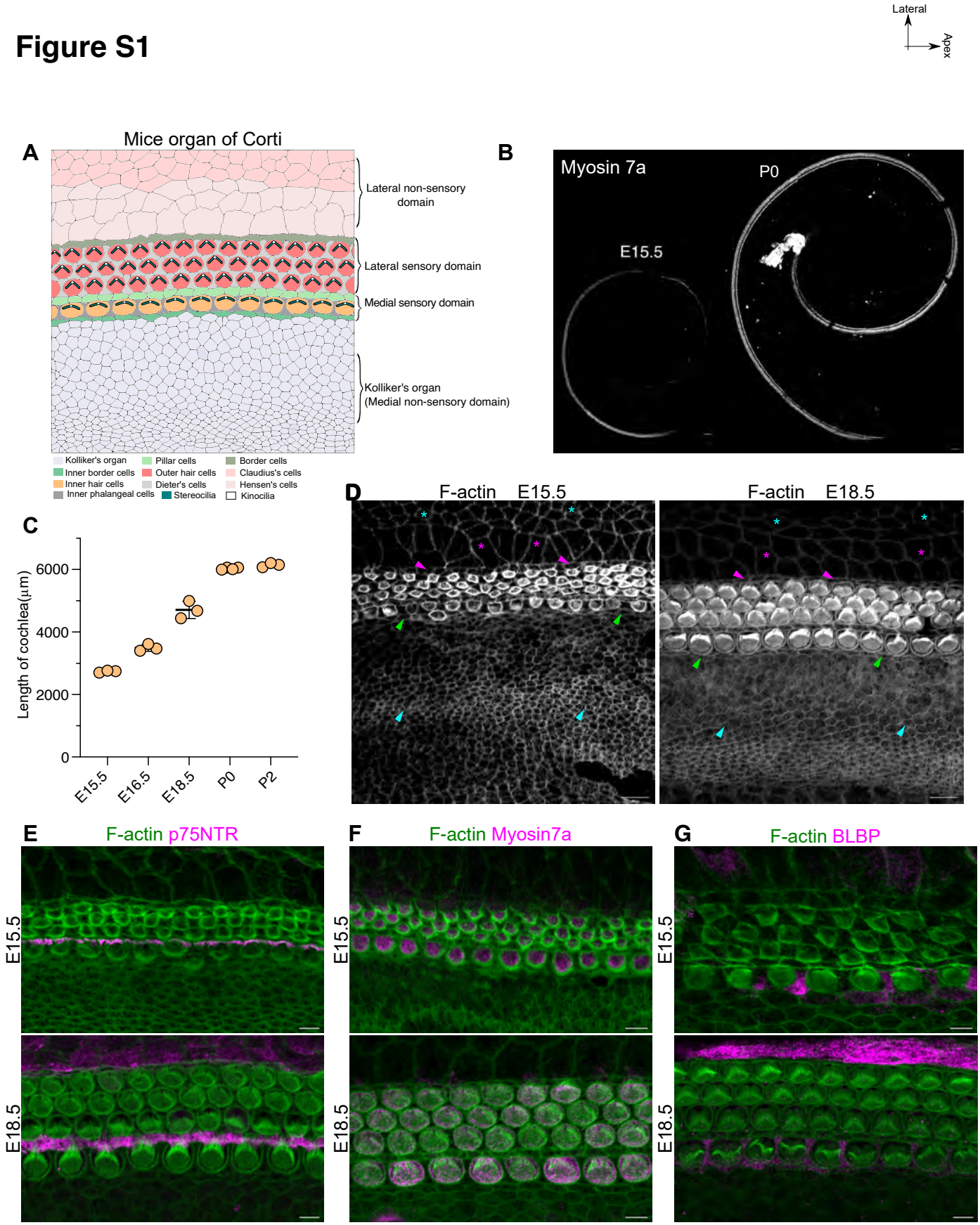

Cellular organisation is maintained during convergent extension mediated elongation of OC.

Figure S2

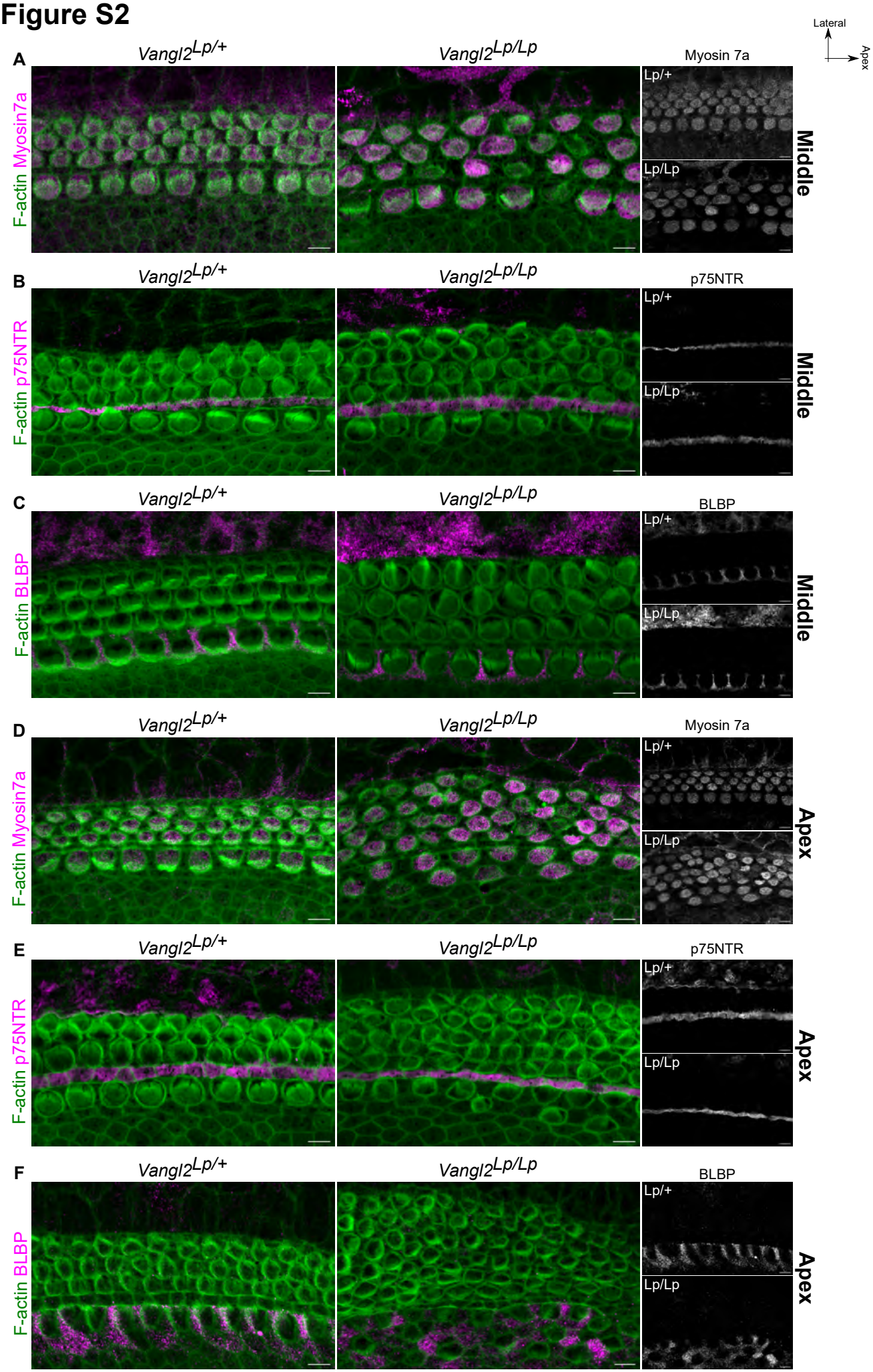

Cellular organisation is preserved in the middle and apex part of looptail mutant OC with defective convergent extension.

Figure S3

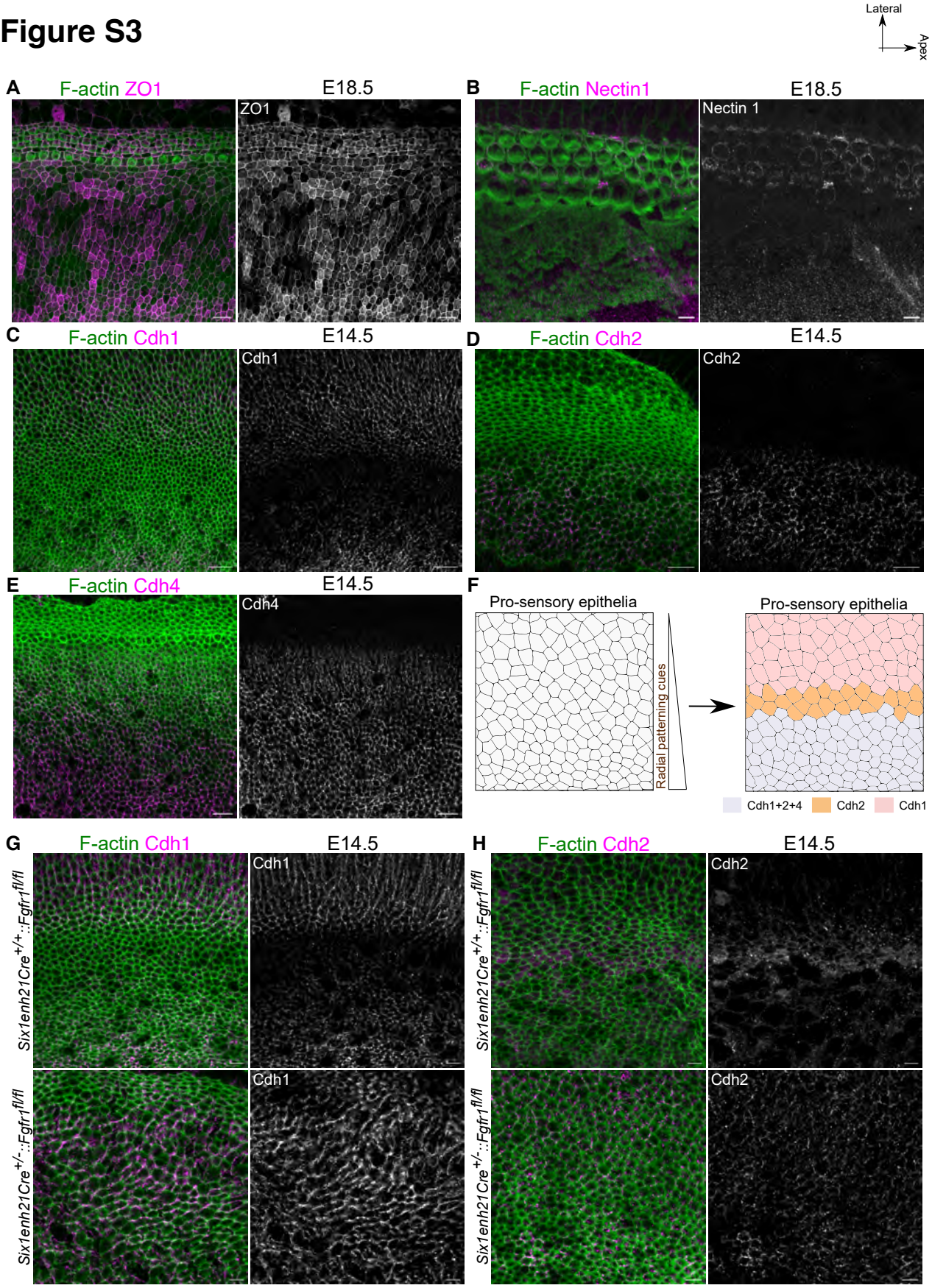

Radial patterning cues regulate development of adhesion-code.

Figure S4

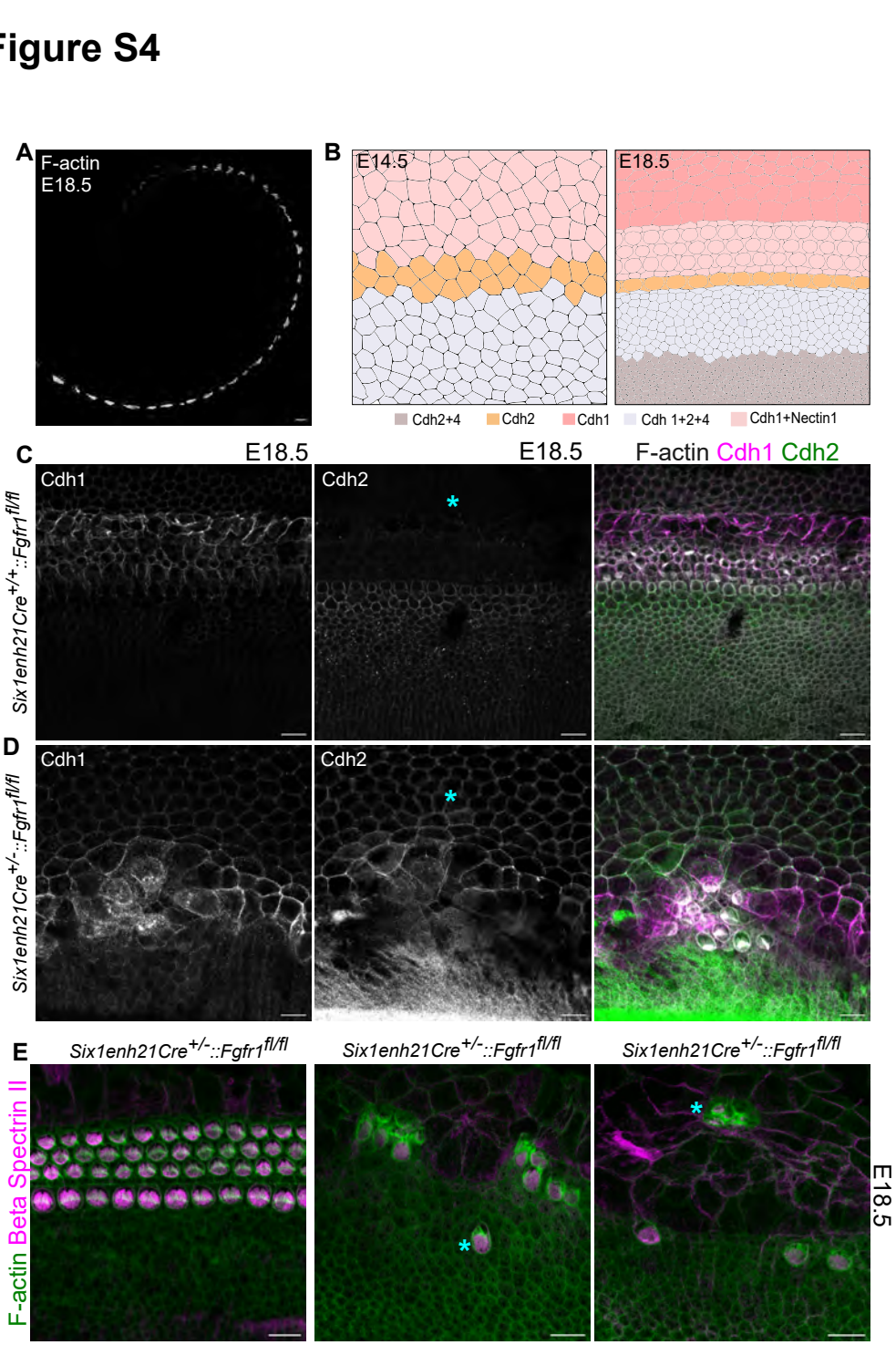

Disruption of Fgfr1 signalling leads to disruption of adhesion code and cellular organisation in mouse OC.

Figure S5

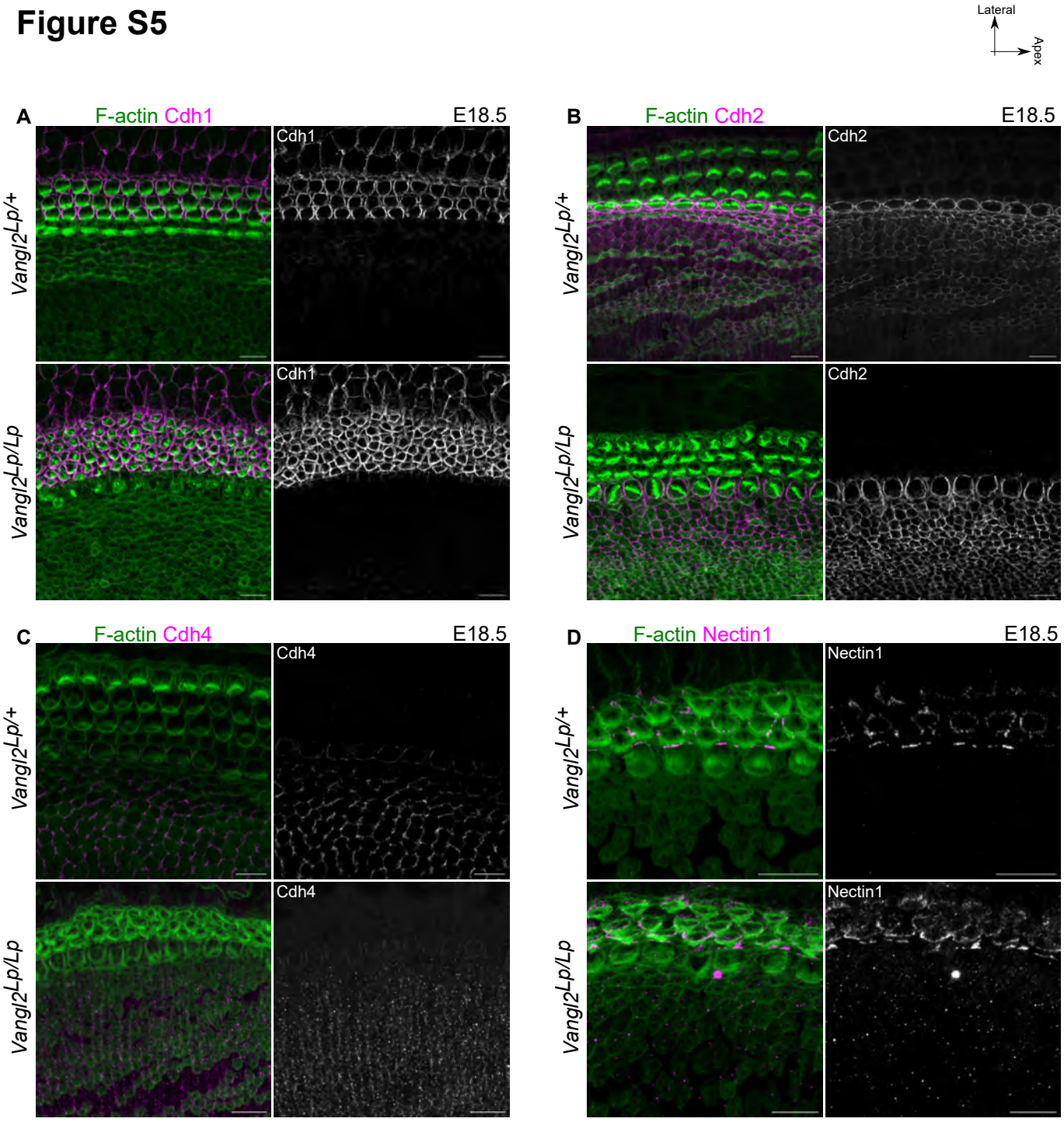

Adhesion code is maintained in looptail mutants with defective convergent extension.

Figure S6

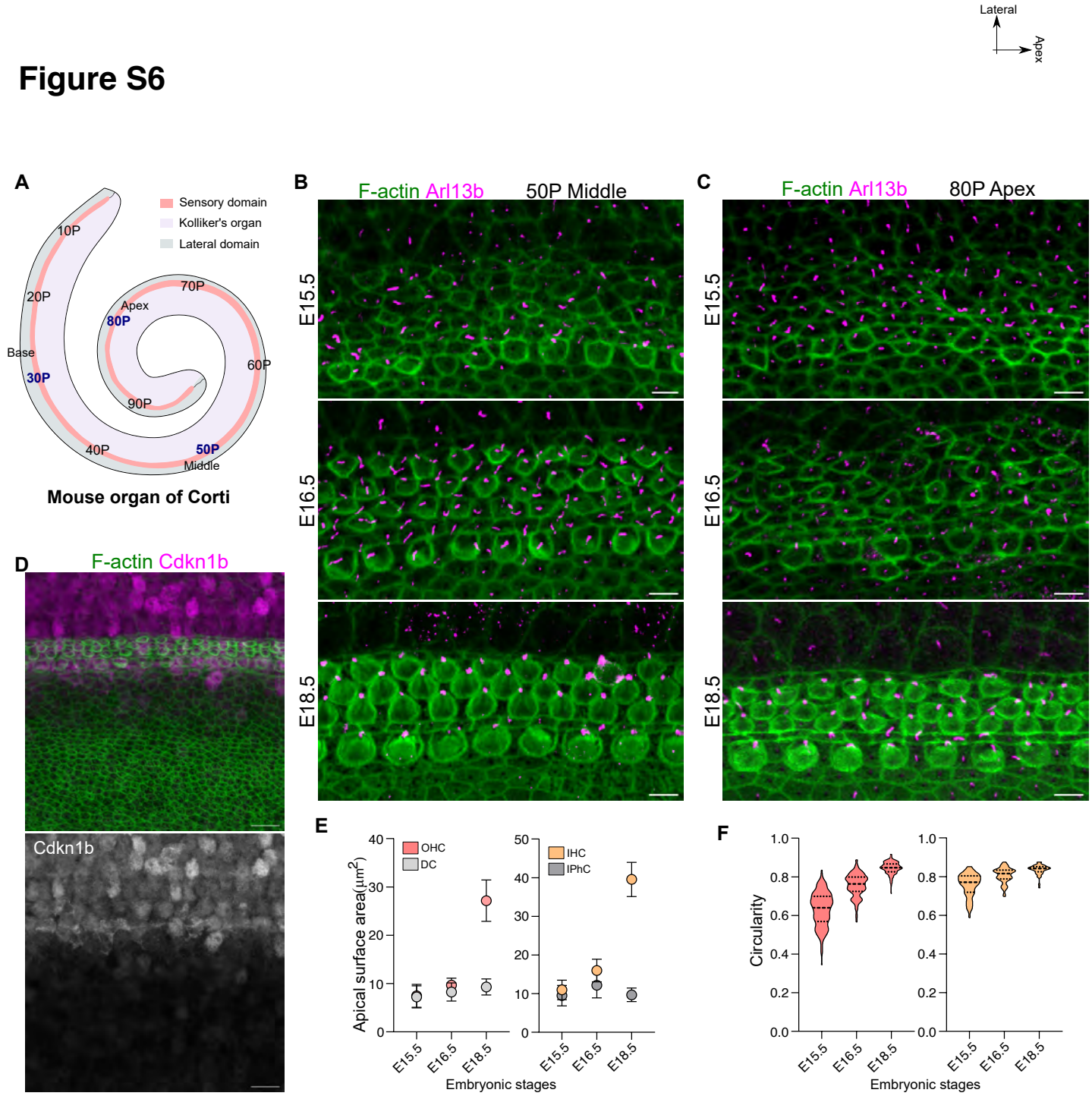

Medial and Lateral sensory domain acquires cellular organisation during development.

Figure S7

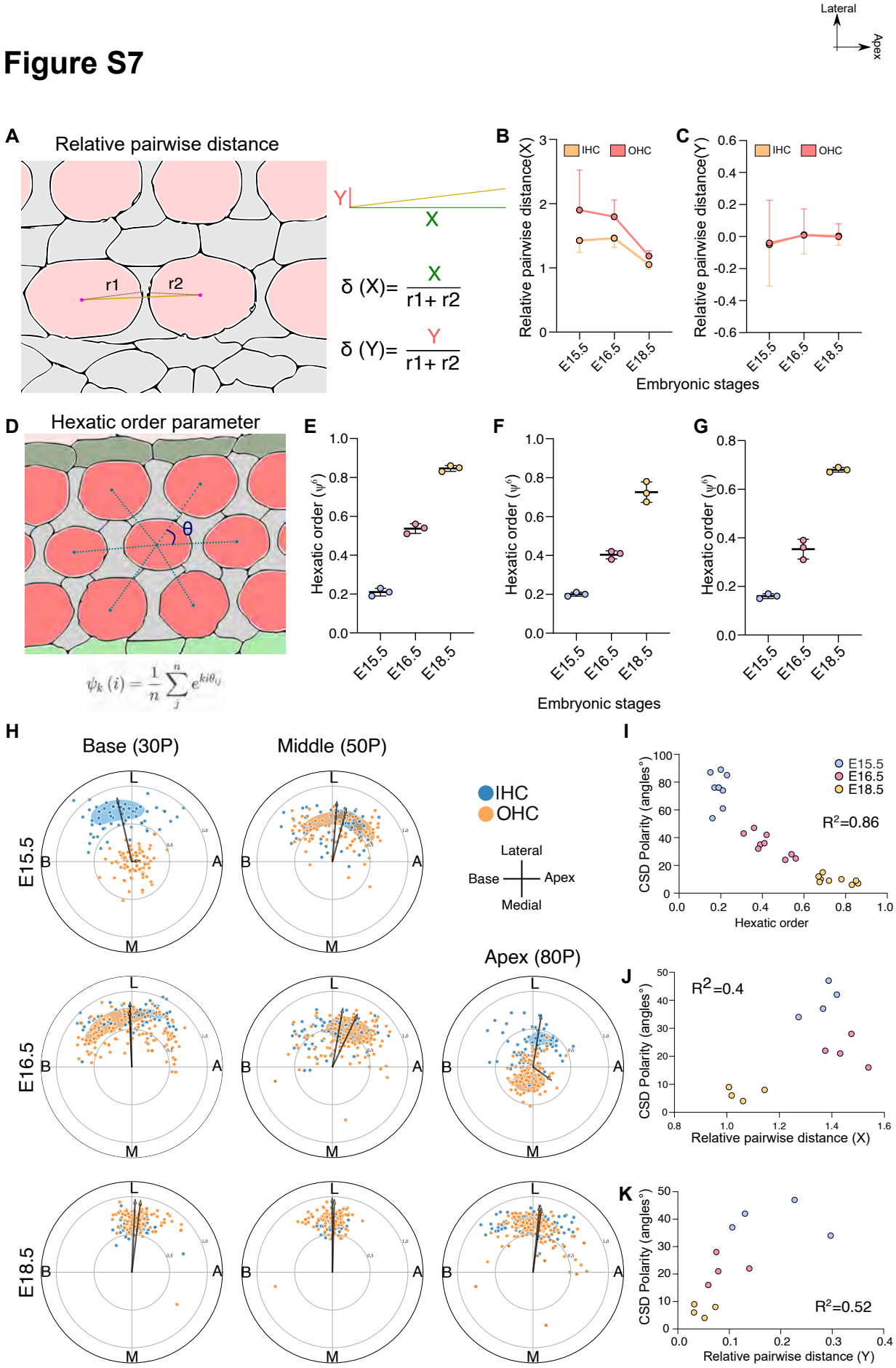

Concurrent development of spatial and orientational order in medial and lateral sensory domain.

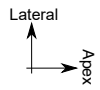

Figure S8

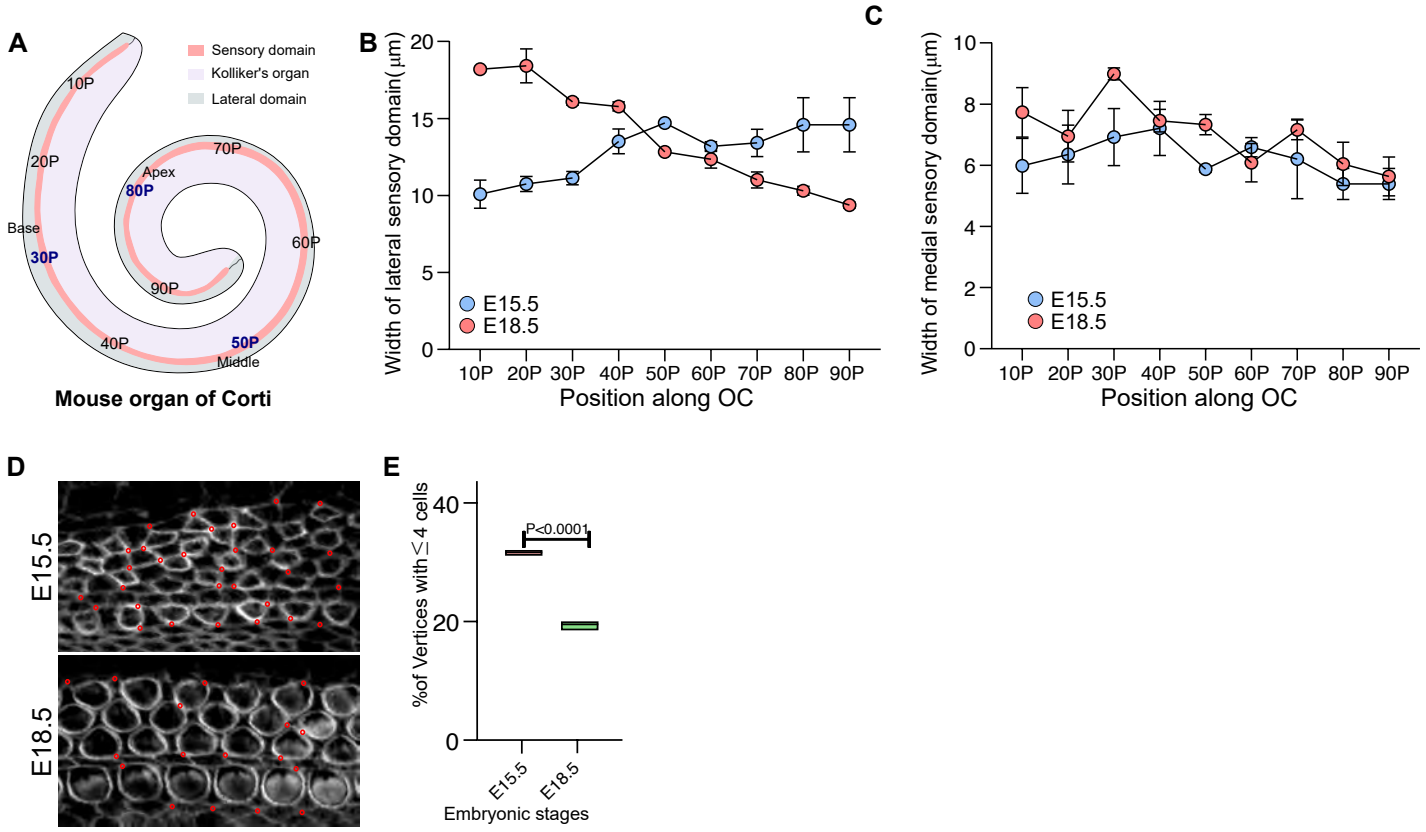

Cellular rearrangement driven elongation of medial and lateral sensory domain.

Supplementary Figure S9

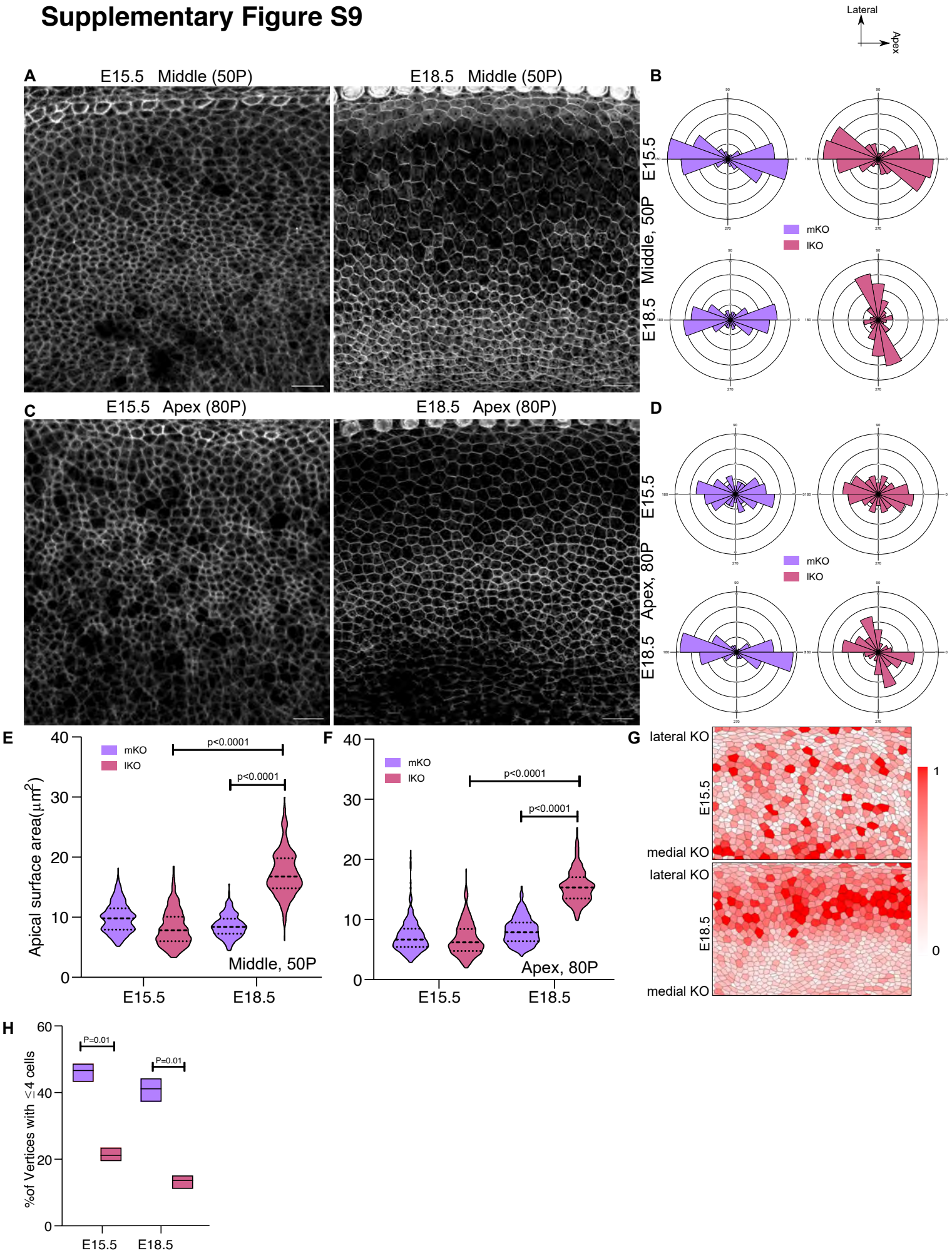

Medial and lateral KÖlliker's organ develops spatial ordering during development.

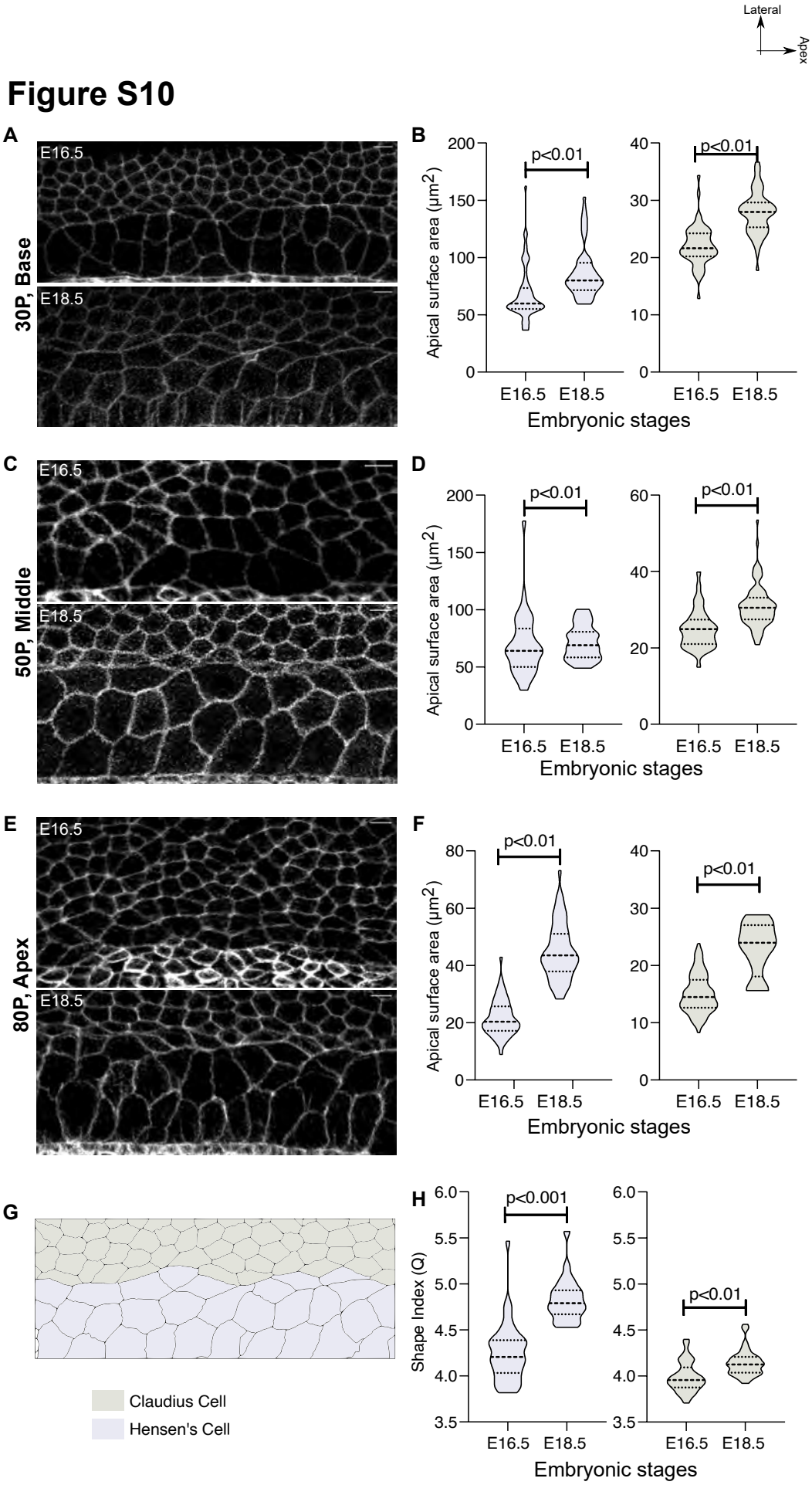

Cells of lateral non-sensory domain increases in apical surface area during development.

Figure S11

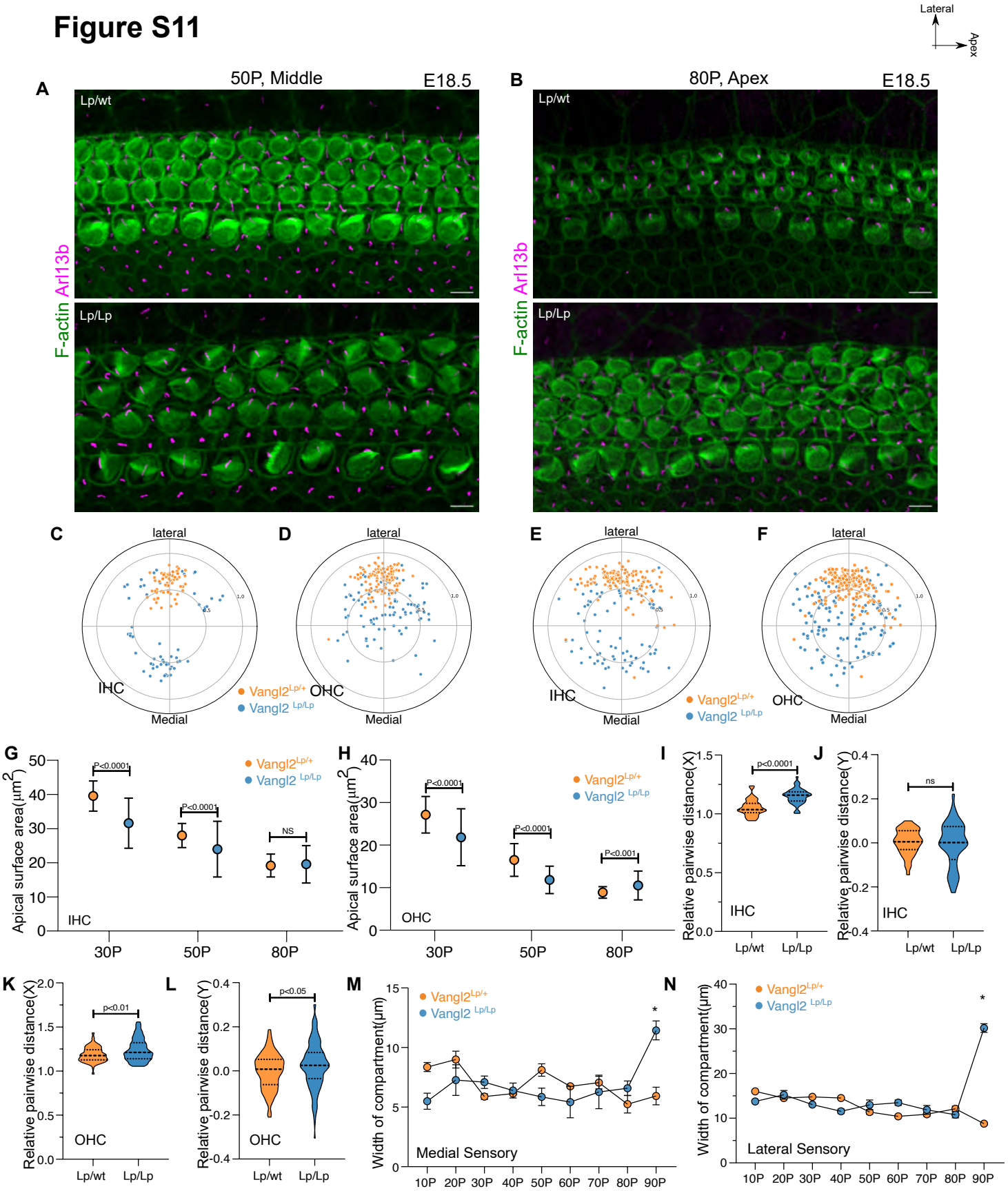

Looptail mutant disrupts spatial and orientational order of sensory compartment.

Figure S12

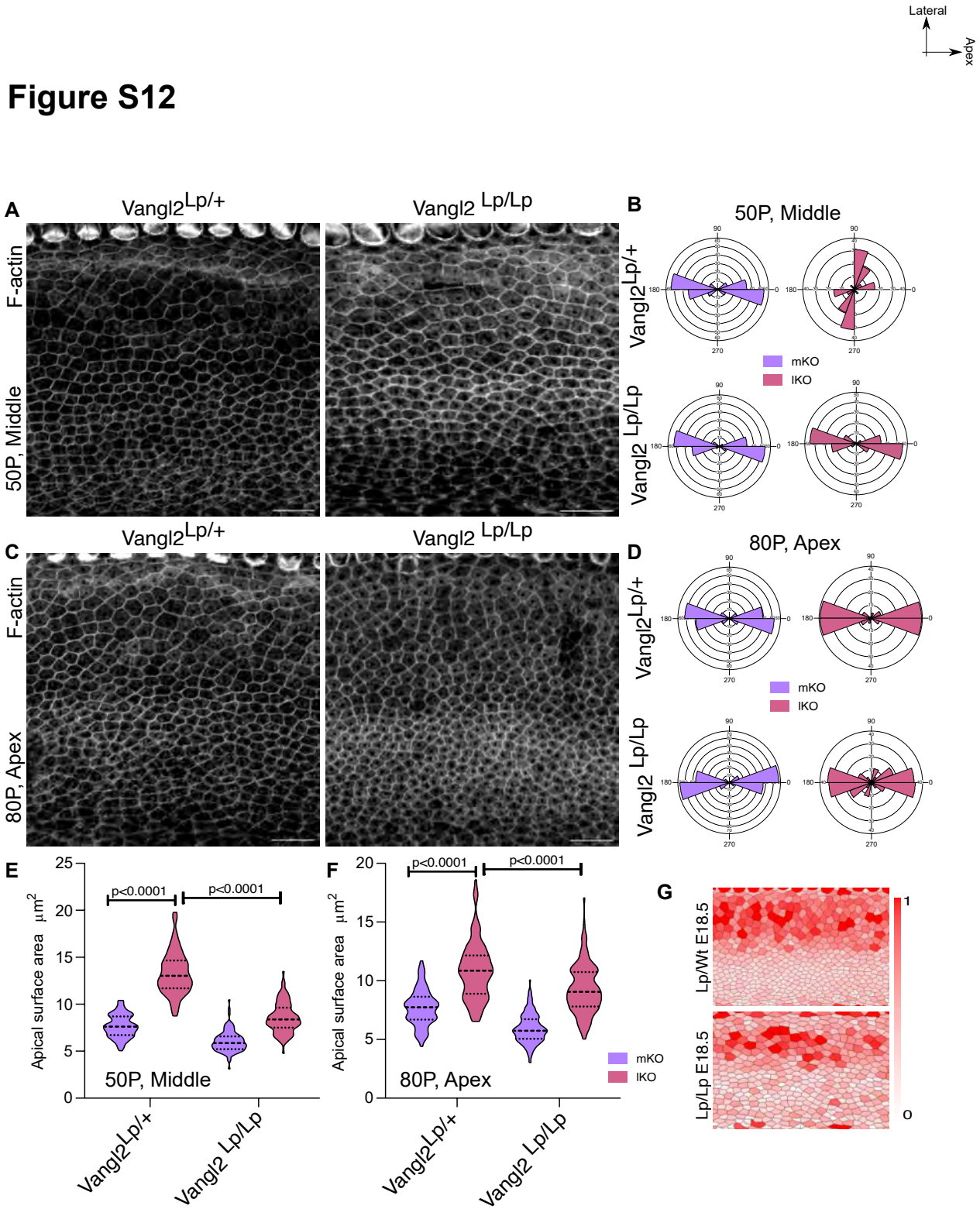

Looptail mutant disrupts cellular organisation in Kölliker's organ.

Figure S13

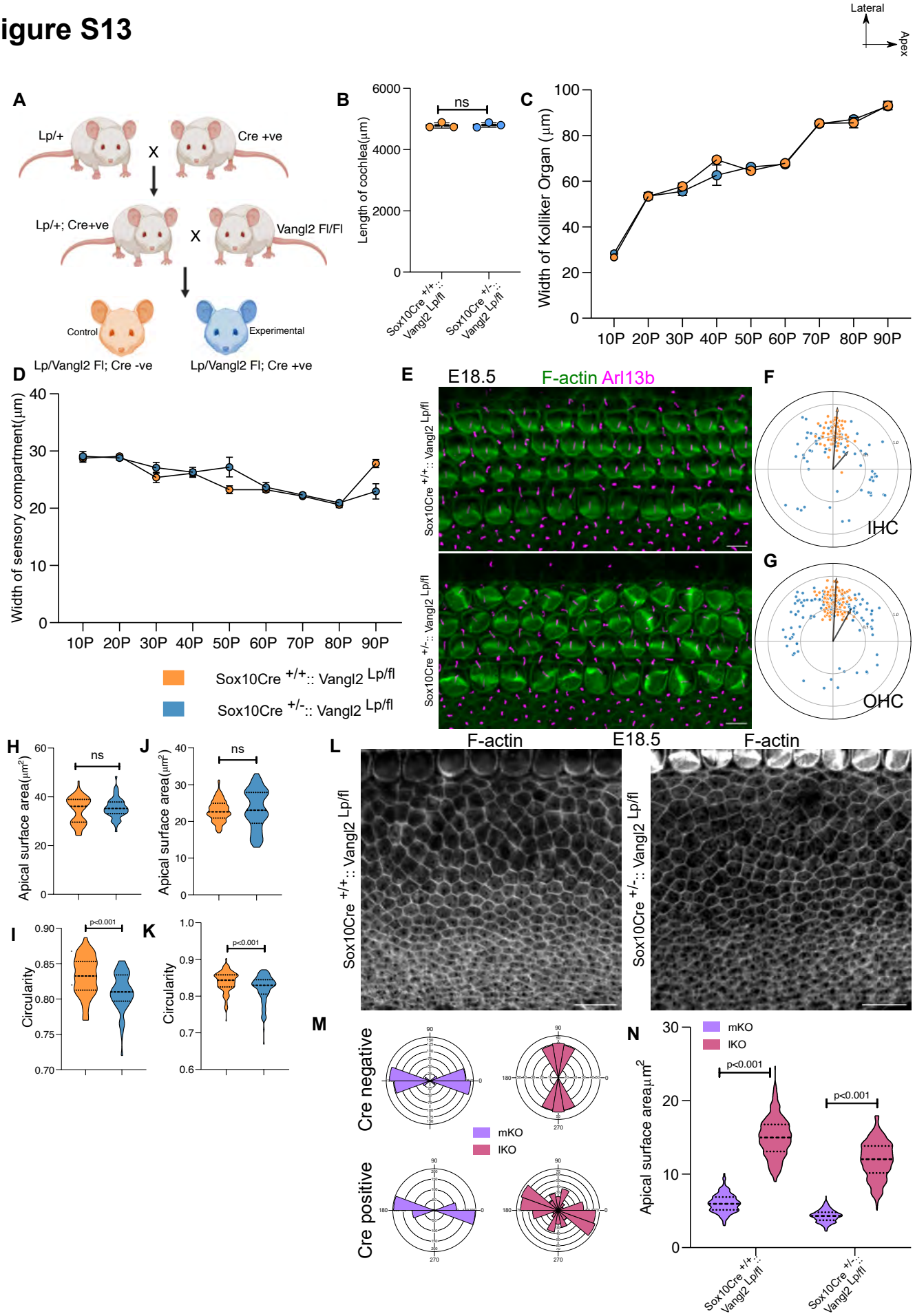

Conditional knockout of Vangl2 from inner ear disrupts cellular organisation in compartments with limited effect on domain sculpting.

Figure S14

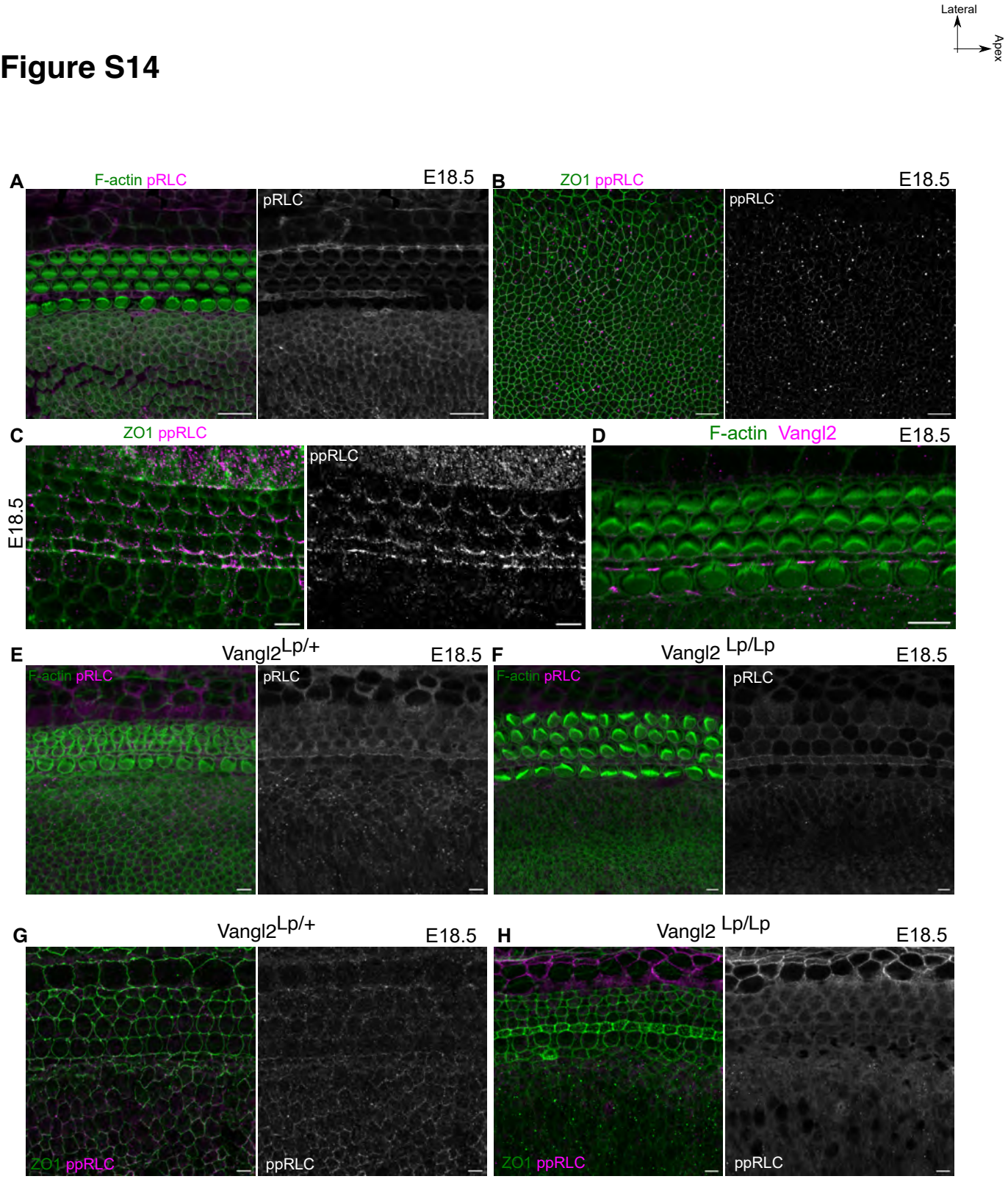

Vangl2 regulates NMII activity through RLC phosphorylation.

Figure S15

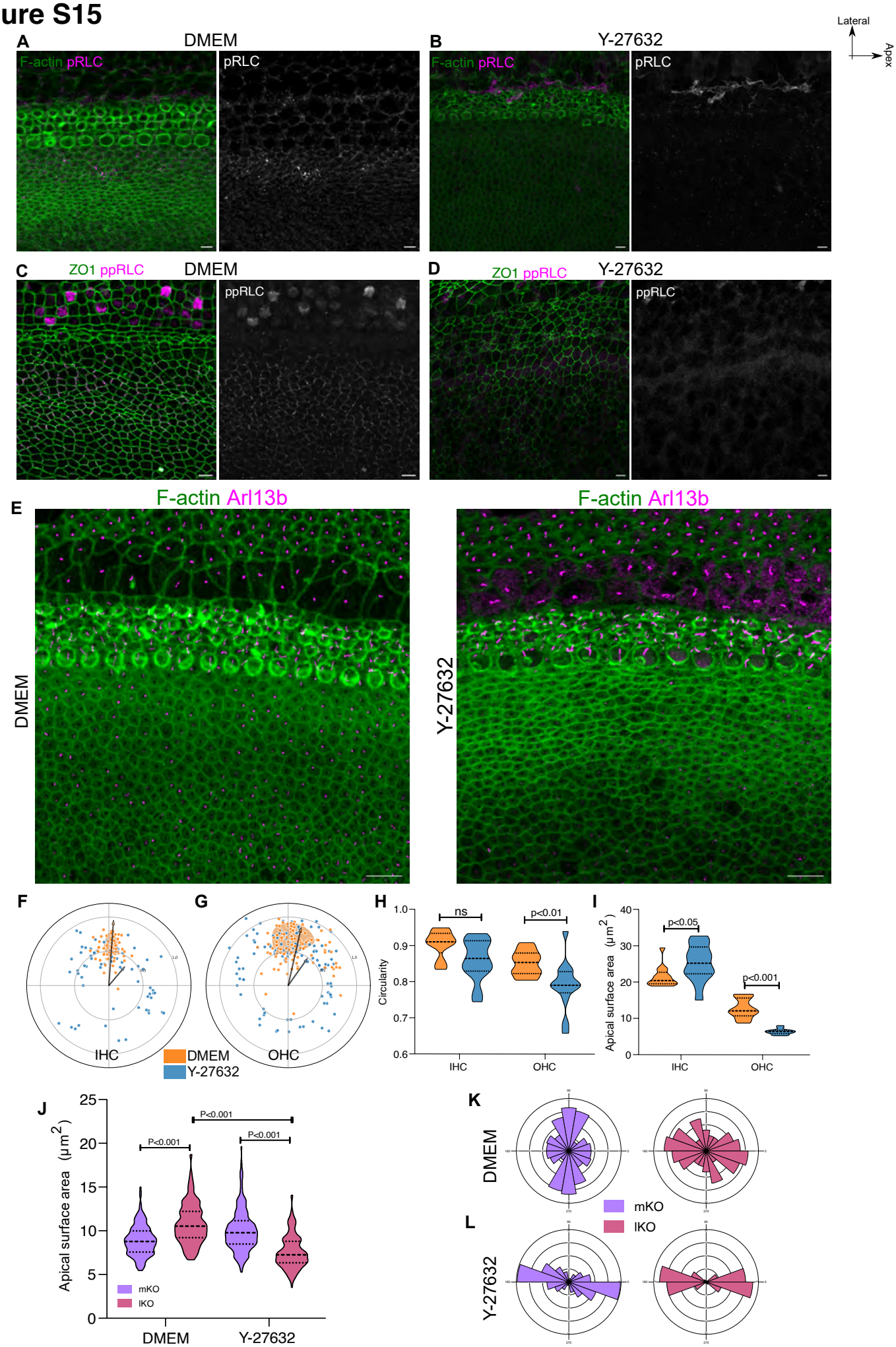

ROCK inhibition disrupts the spatial and orientational order of OC.

Figure S16

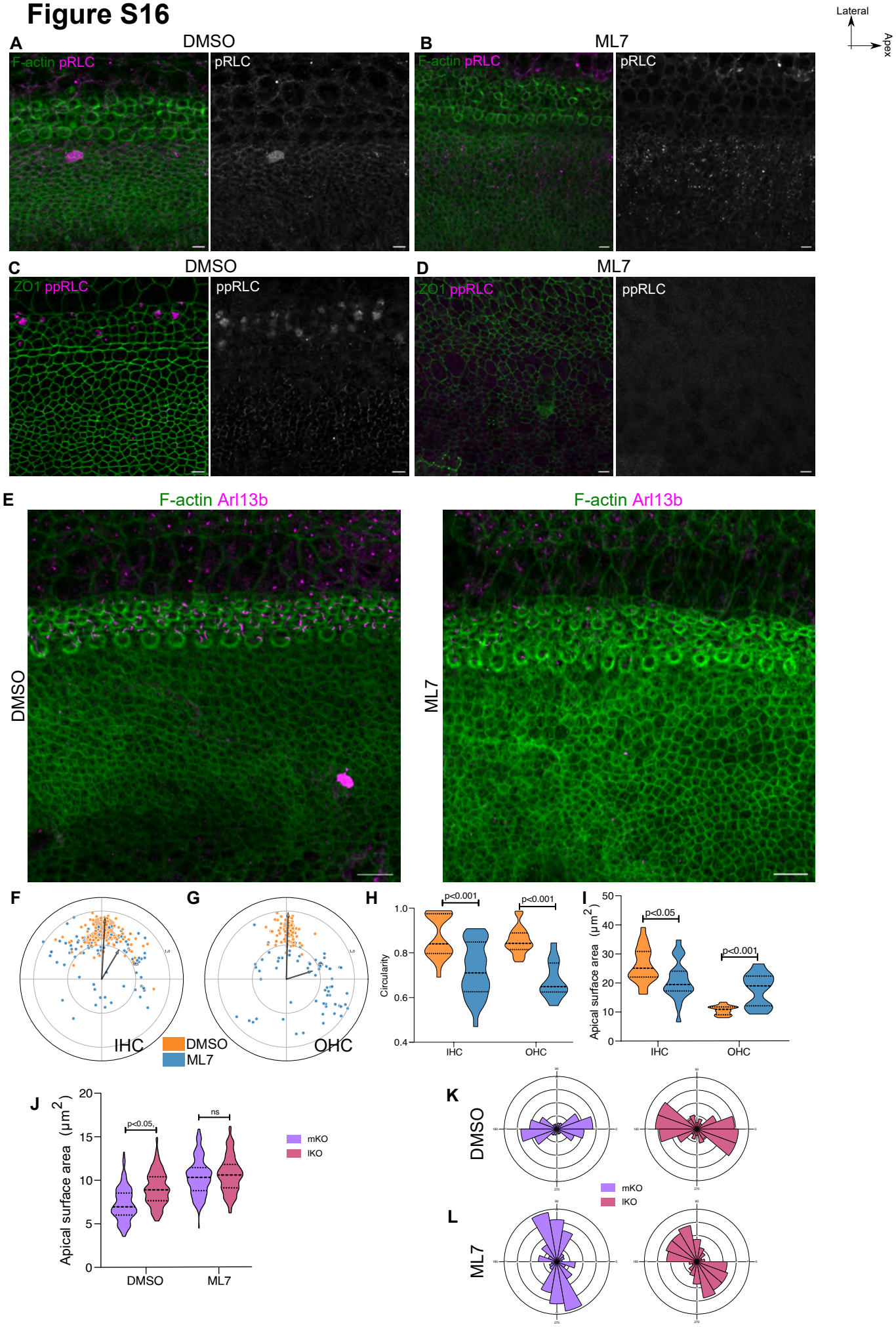

MLCK inhibition disrupts the spatial and orientational order of OC.